

Proximate deconfined quantum critical point in $\text{SrCu}_2(\text{BO}_3)_2$

Yi Cui,^{1,*} Lu Liu,^{2,3,*} Huihang Lin,^{1,*} Kai-Hsin Wu,⁴ Wenshan Hong,² Xuefei Liu,¹ Cong Li,¹
Ze Hu,¹ Ning Xi,¹ Shiliang Li,^{2,5,6} Rong Yu,^{1,†} Anders W. Sandvik,^{4,2,‡} and Weiqiang Yu^{1,§}

¹*Department of Physics and Beijing Key Laboratory of Opto-electronic Functional Materials & Micro-nano Devices, Renmin University of China, Beijing, 100872, China*

²*Beijing National Laboratory for Condensed Matter Physics and Institute of Physics, Chinese Academy of Sciences, Beijing, 100190, China*

³*School of Physics, Beijing Institute of Technology, Beijing 100081, China*

⁴*Department of Physics, Boston University, 590 Commonwealth Avenue, Boston, Massachusetts 02215, USA*

⁵*School of Physical Sciences, Graduate University of the Chinese Academy of Sciences, Beijing, 100190, China*

⁶*Songshan Lake Materials Laboratory, Dongguan, Guangdong 523808, China*

(Dated: October 20, 2022)

The deconfined quantum critical point (DQCP) represents a paradigm shift in quantum matter studies, presenting a “beyond Landau” scenario for order–order transitions. Its experimental realization, however, has remained elusive. Using high-pressure ¹¹B NMR measurements on the quantum magnet $\text{SrCu}_2(\text{BO}_3)_2$, we here demonstrate a magnetic-field induced plaquette-singlet to antiferromagnetic transition above 1.8 GPa at a remarkably low temperature, $T_c \simeq 0.07$ K. First-order signatures of the transition weaken with increasing pressure, and we observe quantum critical scaling at the highest pressure, 2.4 GPa. Supported by model calculations, we suggest that these observations can be explained by a proximate DQCP inducing critical quantum fluctuations and emergent $\text{O}(3)$ symmetry of the order parameters. Our findings take the DQCP from a theoretical concept to a concrete experimental platform.

Introduction.—The theoretically proposed deconfined quantum critical point (DQCP) [1] connects two different ordered ground states of quantum matter by a continuous quantum phase transition (QPT). This type of criticality, which has been explored primarily in the context of two-dimensional (2D) quantum magnets [2], lies beyond the conventional paradigm of discontinuous (first-order) transitions between ordered phases with unrelated symmetries. The DQCP is associated with unconventional phenomena including fractional spinon excitations and deconfined gauge fluctuations [3–5], and further intensive investigations have introduced emergent symmetries [6–11] and exotic first-order transitions [12, 13]. In a very recent extended scenario, the DQCP is a multi-critical point [14, 15] connected to a gapless quantum spin liquid (QSL) [16–20].

Although DQCP phenomena are broadly relevant in quantum materials [21], there has been no positive experimental identification in any system. Quantum magnets in which the interactions can be varied over a wide enough range to realize two phases bordering a DQCP are rare. An exception is the layered material $\text{SrCu}_2(\text{BO}_3)_2$ [22–24], where antiferromagnetic (AFM) Heisenberg interactions between the $S = 1/2$ Cu^{2+} spins (Fig. 1a) provide a remarkably faithful realization of the 2D Shastry-Sutherland model (SSM) [25], in which three different $T = 0$ phases are well established versus the ratio

$g = J/J'$ of the inter- to intra-dimer couplings [26, 27]: an exact dimer-singlet phase (DS, with singlets on the J' bonds), a two-fold degenerate plaquette-singlet (PS) phase (Fig. 1b), and a Néel AFM phase (Fig. 1c). At ambient pressure, $\text{SrCu}_2(\text{BO}_3)_2$ is well described by the $g \simeq 0.63$ SSM with DS ground state [24]. An applied pressure increases g , driving the system into a PS phase at $P \simeq 1.8$ GPa [28, 29], which persists with transition temperature $T_P \simeq 2$ K up to $P \simeq 2.6$ GPa [30, 31]. An AFM phase with T_N from 2.5 to 4 K has been detected between 3.2 and 4 GPa [30].

Here we report a ¹¹B NMR study of $\text{SrCu}_2(\text{BO}_3)_2$ in a magnetic field H up to 15 T and pressures up to 2.4 GPa, with the main goal to characterize the field-driven PS–AFM transition. As Fig. 1d shows at 2.1 GPa, PS and AFM transitions are resolved using their NMR signatures and merge at $H_c \simeq 6$ T and $T_c \simeq 0.07$ K. Such a low T_c in relation to T_P and T_N further away from H_c indicates proximity to a $T_c = 0$ QPT. First-order discontinuities at (H_c, T_c) weaken with increasing pressure, and we observe quantum-critical scaling of the spin-lattice relaxation at 2.4 GPa for $T > T_c$.

Our results support the existence of a multi-critical DQCP controlling the quantum fluctuations at 2.4 GPa, with T_c on the associated first-order line suppressed by an emergent $\text{O}(3)$ symmetry of the combined scalar PS and $\text{O}(2)$ AFM order parameters [7, 8]. By synthesizing past and present experiments on $\text{SrCu}_2(\text{BO}_3)_2$ and model calculations, we arrive at the global phase diagram depicted in Fig. 2. Before further discussing the DQCP scenario, we present our NMR detection of the various phases and transitions.

NMR identification of phases.— We performed

* These authors contributed equally to this study.

† rong.yu@ruc.edu.cn

‡ sandvik@bu.edu

§ wqyu.phy@ruc.edu.cn

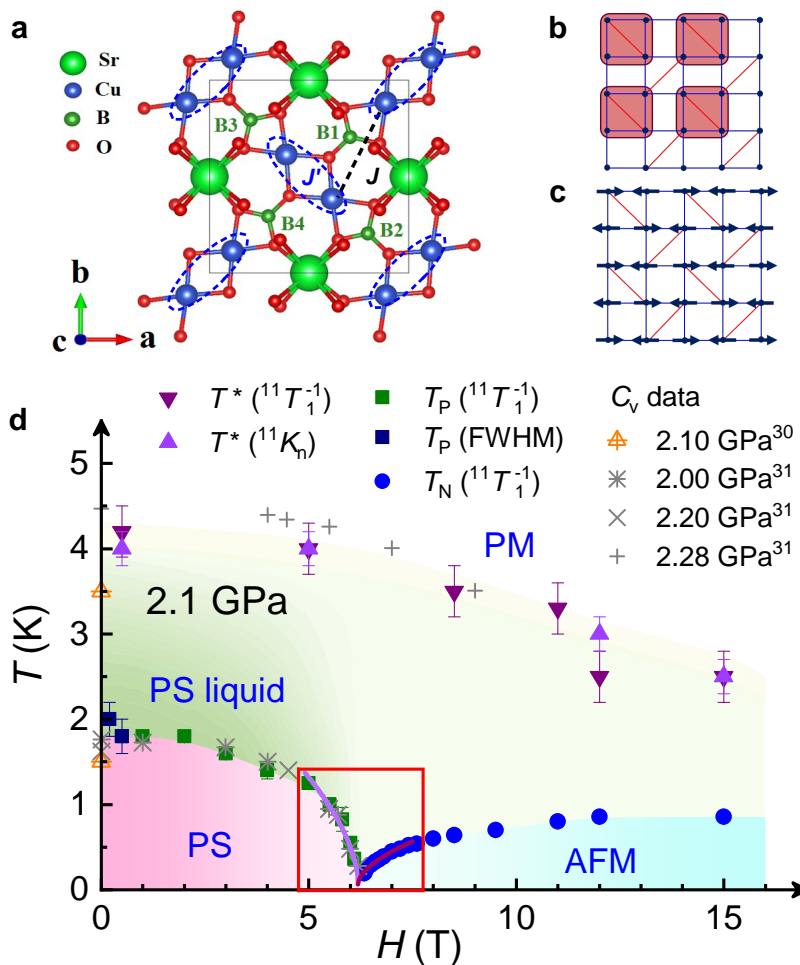


Figure 1. **Experimental overview.** **a** Atomic structure of a $\text{SrCu}_2(\text{BO}_3)_2$ plane. Pairs of Cu^{2+} ions form spin dimers (ellipses) with Heisenberg intra-dimer (J') and inter-dimer (J) interactions (black dashed lines). Each unit cell contains four B ions, whose NMR response we investigate. **b** The PS phase in the equivalent square lattice of J (blue) and J' bonds (red). In $\text{SrCu}_2(\text{BO}_3)_2$, the singlets (shading) form on the full (J') plaquettes, in one of two symmetry-equivalent patterns, while in the SSM the singlets form on the empty plaquettes. **c** The AFM phase, which breaks $O(3)$ symmetry when $H = 0$ and $O(2)$ when $H \neq 0$. For $\text{SrCu}_2(\text{BO}_3)_2$ in a c -axis field, we find that the moments order along the a or b axis. **d** Field-temperature phase diagram at 2.1 GPa, showing the paramagnetic (PM), PS liquid, ordered PS, and AFM phases resolved by our NMR measurements (Figs. 3–5). The transition temperatures T_P and T_N , and the crossover temperature T^* , are compared with specific-heat measurements [30, 31]. The red box marks the regime analyzed in Fig. 5f.

^{11}B NMR measurements on $\text{SrCu}_2(\text{BO}_3)_2$ single crystals at pressures up to 2.4 GPa in fields between 0.2 and 15 T and temperatures down to 0.07 K. Experimental details are provided in Methods [33]. We first discuss NMR line shifts to detect the relevant quantum phases and transitions, followed by results for the spin-lattice relaxation rate $1/T_1$.

A typical ^{11}B NMR spectrum, shown in Fig. 3a, has a central peak with four satellite peaks on either side, from inequivalent sites B1-B4 (Fig. 1a) due to a small tilt angle between field and crystalline c axis (Methods [33]). The satellites are sensitive to changes of the lattice structure because of the local coupling between the nuclear quadrupole moment and the electric-field gradi-

ent (Methods [33]). As shown at a low field and $P = 2.1$ GPa in Fig. 3b, the full-width at half maximum (FWHM) height of the satellites increases on cooling below 10 K until a maximum at $T \simeq 3$ K, reflecting increasing lattice fluctuations when the spins form fluctuating plaquette singlets above the ordered PS phase [31]. This PS liquid crosses over to the trivial PM state at higher temperature.

Below 1.8 K, the FWHM in Fig. 3b rises sharply and saturates around 1 K. As explained in Supplemental Information (SI) Sec. S2 [33], the rapid broadening follows from an orthogonal lattice distortion when a full-plaquette (FP) PS state (Fig. 1b) forms. The FWHM as a proxy for the PS order parameter is further corrobo-

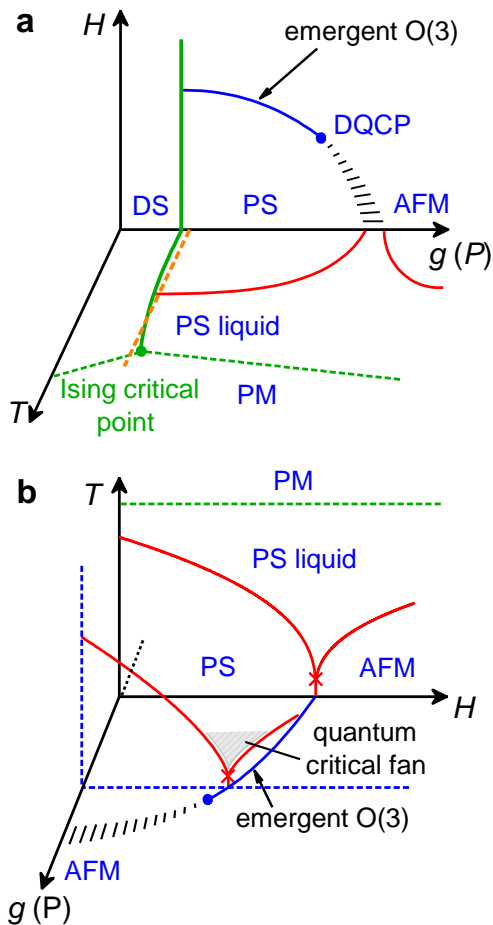


Figure 2. Schematic phase diagram and DQCP scenario. **a** Phases in the space of coupling [$g = J/J'$ in the SSM, P in $\text{SrCu}_2(\text{BO}_3)_2$], temperature, and magnetic field. A multi-critical DQCP separates a line of first-order QPTs and either a QSL phase [17] or a line of generic DQCPs [38]; the region marked with dashed lines represents this undetermined feature. The first-order DS transition (solid green line) terminates at an Ising critical point (green circle) [31]. The green dashed lines indicate crossovers at $T^*(g)$ into the PM phase. The dashed orange line shows how the slightly curved first-order DS transition line can be crossed vs T at fixed P . The ordered AFM phase at $T > 0$ requires inter-layer couplings, as in $\text{SrCu}_2(\text{BO}_3)_2$. The magnetization plateau states at larger H [28, 32] are not shown. **b** Phase diagram drawn to highlight (H, T) planes exemplified by Fig. 1d. Red crosses indicate $T_c > 0$ caused by weak 3D effects and violations of $O(3)$ symmetry. The shading represents the “fan” in which quantum critical scaling is expected. The blue dashed lines indicate the plane of highest-pressure (2.4 GPa) measurements.

rated by the consistency of $T_P \simeq 1.8$ K at the low field applied in Fig. 3b with the location of a sharp specific-heat peak [30, 31], marked in Fig. 1d.

Figure 3c shows the evolution of the central peak with T at $P = 0.9$ GPa and $H = 4$ T. The negative Knight shift at the higher temperatures reflects the hyperfine

coupling $A_{\text{hf}} \simeq -0.259$ T/ μ_B (SI, Sec. S3 [33]) for $\vec{H} \parallel \hat{c}$ [34, 35]. The shift increases rapidly below $T^* \simeq 7$ K when dimer singlets form in the DS state. At 2.1 GPa, Fig. 3e, PS order forms below 2 K but the Knight shift changes rapidly at $T \simeq 4$ K also in this case when the PS liquid forms.

The first-order transition between the DS phase and the PS or PS liquid phase terminates at an Ising-type critical point, which at $H = 0$ is located at $P \simeq 1.9$ GPa, $T \simeq 3.3$ K [31]. At low T , the DS–PS transition takes place between 1.7 and 1.8 GPa [30]. The first-order DS line must therefore bend slightly, as indicated in Fig. 2a, and can be crossed versus T at fixed P . Indeed, at 1.85 GPa, Fig. 3d, the central peak between 3 and 4 K is split, indicating phase coexistence. Previously a different splitting was reported at 2.4 GPa [35, 36], perhaps caused by pressure inhomogeneity, but we observe the double peak only at 1.85 and 1.95 GPa (SI, Sec. S3 [33]). Outside this pressure range, T^* likely only marks a rapid crossover between the PM and PS liquid, whose associated sharp specific-heat peaks [30, 31] can be explained by an analogy [31] with the Widom line away from the gas–liquid critical point. We have found no NMR signatures of a structural transition here or at higher temperatures (SI Sec. S3 [33]).

Above 1.95 GPa, AFM order emerges at high fields and leads to splitting of the central NMR line by alternating positive and negative hyperfine fields, as shown at 2.1 GPa and 2.4 GPa in Fig. 4a and Fig. 4b, respectively, both at $T = 0.07$ K. The sudden rise with field of the peak-splitting $f_R - f_L$ (a proxy AFM order parameter), shown in Fig. 4c, signals a discontinuous onset of AFM order at $H_c(P)$, with the discontinuity much weaker at the higher pressure.

In the AFM state, the uniform magnetization does not exhibit any obvious discontinuity at H_c and remains below 2% of the saturated moment at our highest field of 15 T (SI, Sec. S4 [33]). A cross-over temperature T^* persists also at high fields, where the PS liquid develops increasing spin fluctuations (discussed further below).

Spin-lattice relaxation rate.— $1/T_1$ is a direct probe of low-energy spin fluctuations and can detect the PS and AFM transitions more precisely than (but consistent with) the line shifts. Figures 5a and 5b show $1/T_1$ at $P = 2.1$ GPa for a wide range of applied fields that we group below and above 6.2 T, corresponding respectively to the low- T PS and AFM phases; Figs. 5c and 5d show the same at 2.4 GPa with the separation at 5.8 T.

At 2.1 GPa, Fig. 5b, we find a sharp drop of $1/T_1$ at $T^* \simeq 3$ –4 K and a broad peak or sharper kink below 2 K. At low fields in Fig. 5a, the latter feature extends to 6.1 T and clearly marks the opening of a spin gap below T_P . At $P = 2.4$ GPa, we do not find a peak at T_P (Fig. 5c) but rather a sharp crossover from a low- T gapped regime to a window with power-law behavior that is analyzed in Fig. 5e and will be further discussed below. At the higher fields in Fig. 5b and 5d, the low- T features (below 0.8 K) are much sharper and coincide with the NMR peak

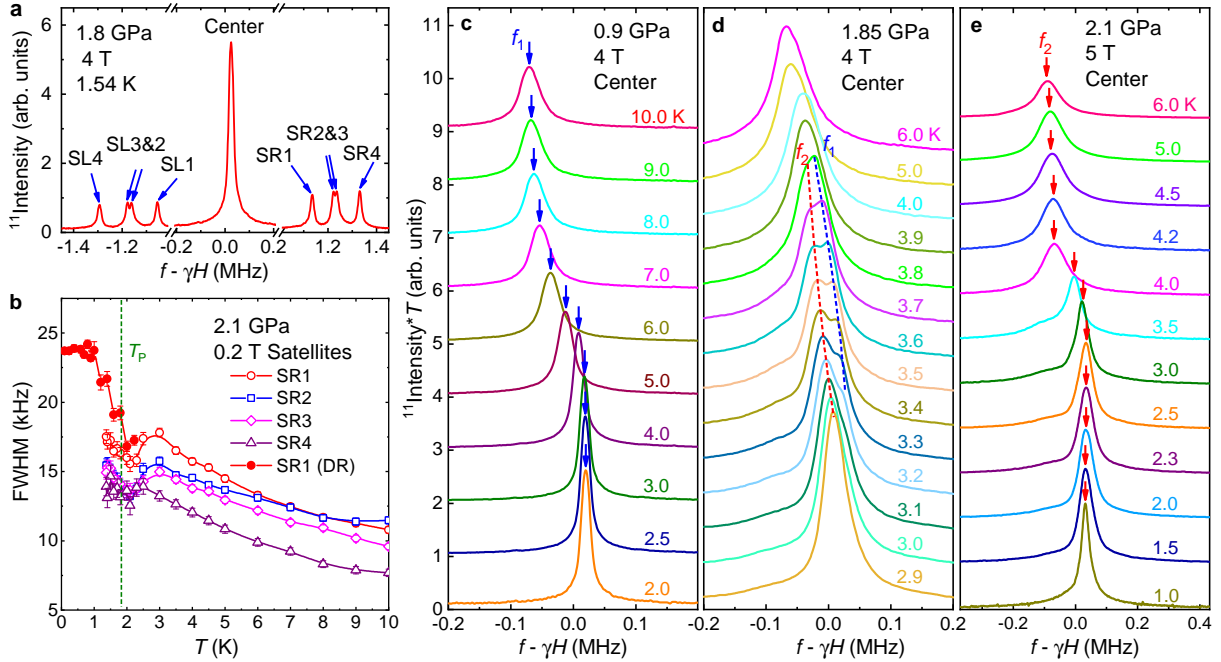


Figure 3. **NMR spectra and line shifts.** **a** NMR ^{11}B spectrum at $H = 4$ T and $P = 1.8$ GPa, with the field applied at 8.6° from the crystalline c axis, showing the center line and two sets of satellites associated with the four B sites (Fig. 1a). **b** FWHM of satellites SR1-SR4 shown as a function of temperature at $P = 2.1$ GPa and $H = 0.2$ T. The line at 1.8 K marks the onset of an upturn with further cooling. SR1 was measured in the dilution refrigerator in addition to the VTI used for all cases (SI Sec. S2 [33]). **c-e** NMR center line for a range of temperatures (curves shifted vertically) at (c) $P = 0.9$ GPa, $H = 4$ T, (d) 1.85 GPa, 4 T, and (e) 2.1 GPa, 5 T. The peaks in the DS phase (c) and in and above the PS phase (e) are marked f_1 and f_2 , respectively. The split peak in (d) reflects phase coexistence.

splitting in Figs. 4a and 4b. Thus, we can safely identify these peaks for $H \geq 6.33$ T as T_N [37]. The minimum in $1/T_1$ around 1.5 K in Fig. 5b increases with the field, indicating increasing spin fluctuations in the PS liquid state.

Figure 5f shows very clear field-induced PS–AFM transitions revealed by these signals at both $P = 2.1$ and 2.4 GPa. The PS and AFM boundaries $T_P(H)$ and $T_N(H)$ meet at a remarkably low T_c . Given phase coexistence (Figs. 4a,b) the quantum phase transition at H_c is clearly first-order. The proxy AFM order parameter $f_R - f_L$ in Fig. 4c is consistent with H_c determined from $1/T_1$ at both pressures. The much smaller first-order discontinuity of $f_R - f_L$ at the higher pressure indicates the approach toward a continuous QPT.

We have extracted the PS spin gap Δ by fitting $1/T_1$ below T_P to a semi-empirical form $T^{-a}e^{-\Delta/k_B T}$ with $a \approx 1$ (SI, Sec. S5 [33]). As expected, a linear decrease with H of Δ at both pressures is revealed in Fig. 6a, on account of the field-lowering of the $S = 1$ ($S^z = 1$) state above the singlet PS ground state. The results are compatible with previously determined $H = 0$ gap estimates [29, 30] and the known g -factor.

At a first-order transition into the AFM phase, the PS gap should jump discontinuously to zero at H_c (given that the AFM state is gapless), but, despite the clear first-order signals described above (Fig. 4c), we find

$\Delta(H_c)$ values indistinguishable from zero within statistical errors. We will discuss the anomalously small gap discontinuity in the context of the proximate DQCP scenario further below.

Deconfined quantum criticality.— The SSM at $H = 0$ has been a candidate for a DQCP separating its coupling-induced PS and AFM ground states [7, 38]. The singlets in the PS phase of the model occupy the empty plaquettes, in contrast to the FP state in $\text{SrCu}_2(\text{BO}_3)_2$ (Fig. 1b). This aspect of the PS state depends sensitively on other possible weak interactions beyond the SSM [11, 39], and the SSM description of the global phase diagram of $\text{SrCu}_2(\text{BO}_3)_2$ should remain valid.

There is mounting evidence that a gapless QSL phase can exist between a PS state (or closely related spontaneously dimerized state) and the AFM state in frustrated 2D quantum spin systems [16, 20, 40–42] and that these QSL phases generically end at multi-critical DQCPs [15, 17, 18]. Beyond such a point, the transition without intervening QSL is expected to be first-order, with the coexistence state at $H = 0$ inheriting (and breaking) the emergent $O(4)$ or $SO(5)$ symmetry (depending on the type of singlet-ordered phase [7, 8, 10, 12, 13]) of the DQCP.

In the $H = 0$ SSM, early calculations indicated a first-order PS–AFM transition [27], and a recent calculation suggested an $O(4)$ [from the $O(3)$ AFM and scalar PS

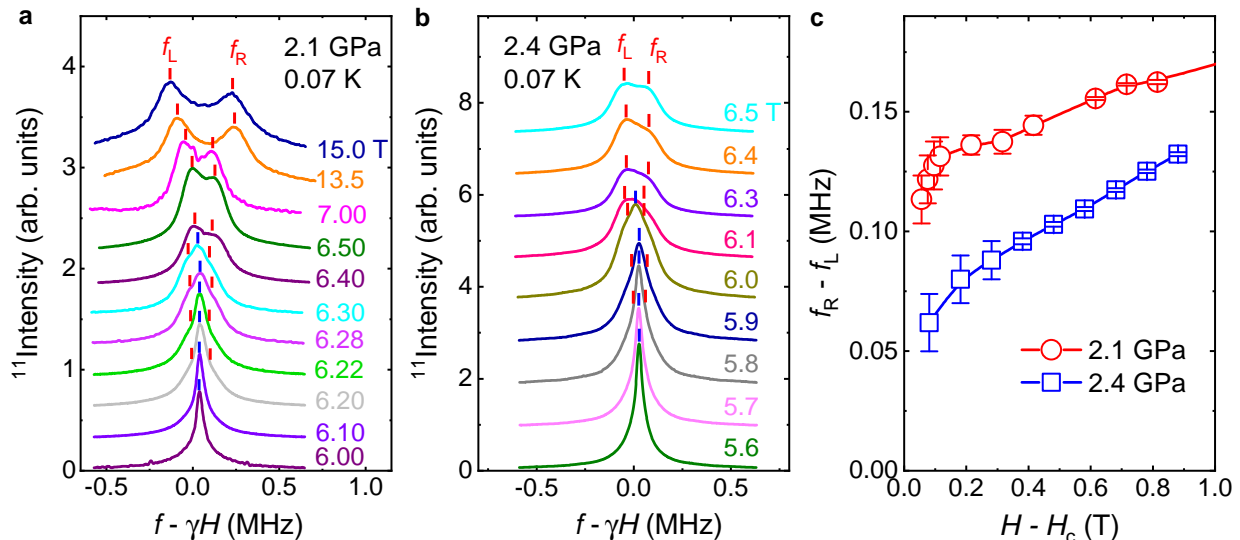


Figure 4. **AFM transition.** Splitting of the NMR center line with increasing H at $T = 0.07$ K is shown in **a** and **b** for $P = 2.1$ GPa and 2.4 GPa, respectively. The two peaks marked f_L and f_R (red bars) indicate AFM order developing above $H \simeq 6$ T. A center peak (blue bars) remaining at slightly higher fields indicate phase coexistence. **c** Proxy AFM order parameter $f_R - f_L$ vs $H - H_c$, where H_c is determined using the spin-lattice relaxation rate (Fig. 5).

order parameters] multi-critical DQCP in an extended parameter space [11]. A generic O(4) DQCP had previously been proposed [38]. The intervening gapless QSL between the PS and AFM phases was identified very recently [17, 19] and may be explained by an instability of the conventional DQCP [15]. These theoretical insights along with our NMR results for $\text{SrCu}_2(\text{BO}_3)_2$ suggest the scenario in Fig. 2. Since no experiment so far (including ours) have explicitly confirmed a QSL phase, the possibility remains that there is instead another line of PS–AFM transitions. Though the dashed regions in the phase diagrams in Fig. 2 can represent either possibility, specific heat measurements at $H = 0$ [30, 31] found no phase transition between 2.6 and 3.2 GPa, consistent with a QSL ground state evolving into the $T > 0$ PS liquid.

A putative multi-critical DQCP at $H > 0$ should evolve from a corresponding $H = 0$ DQCP with emergent O(4) symmetry [7, 38]. While this O(4) point exists only in an extended parameter space outside the (g, H, T) cube in Fig. 2, the fact that the field-induced magnetization is very small at H_c (SI, Sec. S4) suggests that the putative $H > 0$ DQCP still hosts an approximate O(4) symmetry, with stronger O(3) character developing on the first-order line. Strictly speaking, at $H > 0$ the DQCP may evolve into a near-critical triple point with first-order signatures at the lowest energy scales.

Closer proximity of $\text{SrCu}_2(\text{BO}_3)_2$ to some continuous QPT with increasing pressure is certainly supported by our observation of a weaker discontinuity of the AFM order parameter at 2.4 GPa than at 2.1 GPa (Figs. 4c). Moreover, at a clearly first-order transition correspondingly high T_c values would normally be expected. The low T_c at both pressures then point to a mechanism sup-

pressing long-range order also rather far away from the QPT. The DQCP scenario offers this possibility through its emergent continuous symmetry inherited (at least up to some large length scale) by the first-order line. An ideal 2D coexistence state with continuous order parameter symmetry must have $T_c = 0$, but weak violations of the symmetry (in combination with 3D effects [43]) would imply a low $T_c > 0$, as observed in $\text{SrCu}_2(\text{BO}_3)_2$.

In the scenario of a first-order transition with emergent O(3) symmetry, the Ising-type PS order can be understood as an uniaxial deformation of the O(3) order parameter. A logarithmic form of the PS transition temperature is then expected; $T_P \propto \ln^{-1}[a(H_c - H)]$, for some value of a [7, 44]. Fits of the experimental data to this form (SI, Sec. S6 [33]) are shown with solid curves in Fig. 5f and indeed describe the behavior close to H_c .

To describe $T_N(H)$, we note again that inter-layer interactions are required for $T_N > 0$ in a spin-isotropic system. These couplings also change a continuous QPT ($T_c = 0$) into a first-order line extending to a bicritical or triple point at $T_c > 0$ [38, 43] (red crosses in Fig. 2b). Given the extremely low T_c values in $\text{SrCu}_2(\text{BO}_3)_2$, a modified critical form with the same exponent ϕ governing both transitions above T_c may be expected from DQCP dualities [13, 45]: $T_{P,N} = T_c + a_{P,N}|H - H_c|^\phi$. Fits with independent exponents ϕ for the PS and AFM transitions (Sec. S6, SI [33]) indeed support a common value and motivate joint fitting with a single ϕ . Such fits are shown with the dashed curves in Fig. 5, where T_c is in the range 0.05–0.07 K at both pressures. At 2.1 GPa $H_c = 6.184 \pm 0.005$, $\phi = 0.57 \pm 0.03$, while at 2.4 GPa $H_c = 5.719 \pm 0.009$, $\phi = 0.50 \pm 0.03$. These fits, where ϕ is close to estimates for both SO(5) [12, 14] and O(4)

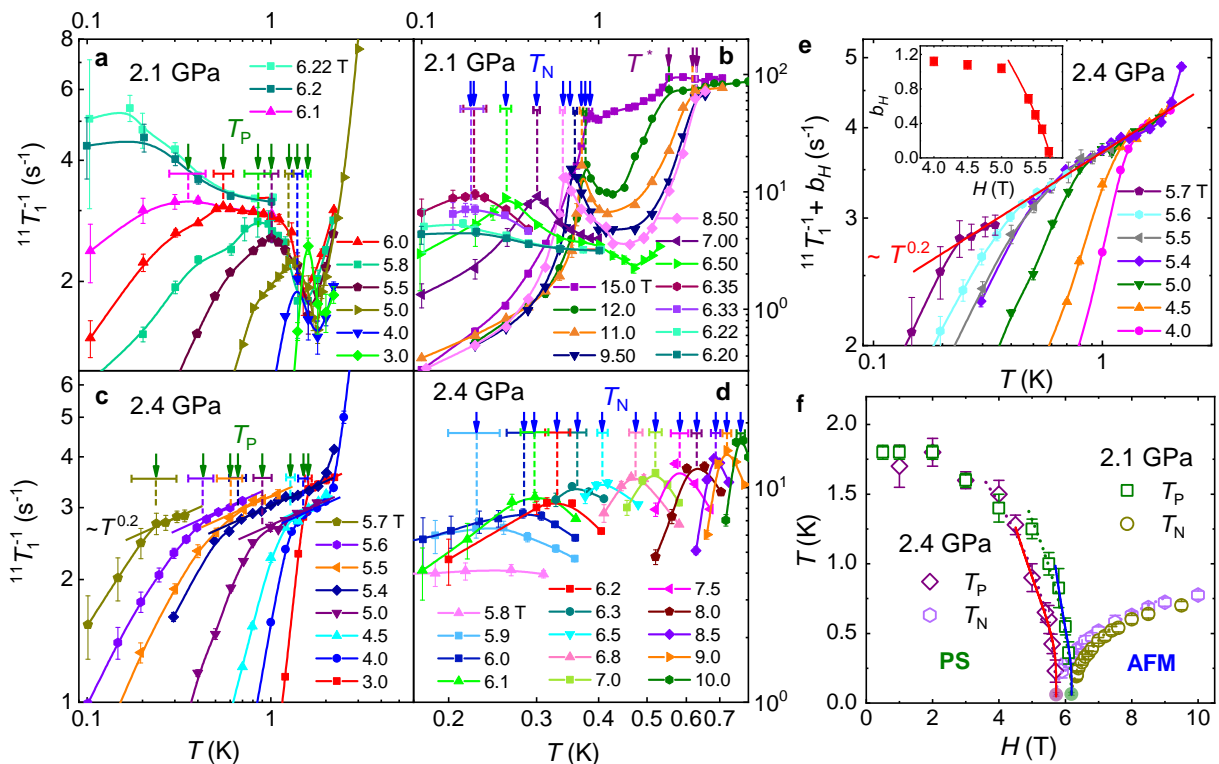


Figure 5. **Spin-lattice relaxation.** $1/^{11}T_1(T)$ measured at 2.1 (a,b) and 2.4 GPa (c,d), separated to show the PS (a,c) and AFM states (b,d). The drop in $1/T_1$ at a $T^* \simeq 4$ K (a,b) indicates the sharp crossover into the PS liquid. The peaks at lower T mark T_P and T_N , with uncertainties indicated by the horizontal bars. At 2.4 GPa, no low- T PS peak is observed (c), but T_P can be extracted from the sudden change from thermally activated to quantum critical behavior, $1/T_1 = aT^\eta - b_H$. Power-law scaling of the offset, $b_H \propto (H_c - H)^d$ with $d \approx 0.8$, close to H_c is shown in the inset of e. The common scaling form with constant a and $\eta \approx 0.2$ is demonstrated in main panel e, where b_H has been added. f Low-temperature phase diagrams at 2.1 and 2.4 GPa. The solid and dotted lines indicate the phase boundaries modeled by respectively, a logarithmic form of T_P and near-critical forms of both T_P and T_N (SI, Sec. S6 [33]). The latter fits give the T_c values indicated with circles.

[45] DQCPs (see further Sec. S6A), do not rule out the alternative logarithmic form of T_P but further validate the very low T_c values and common transition field H_c for both order parameters.

Quantum-critical relaxation.— In Fig. 5c, $1/T_1$ at 2.4 GPa exhibits T^η scaling with $\eta \approx 0.2$ within a window of temperatures for several fields close to H_c on the PS side. The ensemble of fits is further analyzed in Fig. 5e using the expected quantum-critical form $1/T_1 = aT^\eta - b_H$ [46], where a is a constant and $b_H > 0$ for $H < H_c$. The fact that scaling behavior is not observed at 2.1 GPa (Fig. 5a) suggests that only the system at 2.4 GPa is sufficiently close to a continuous QPT that it realizes the quantum critical fan [46], depicted in Fig. 2b, where T is the largest energy scale (but low enough so that the correlation length is well above the lattice constant). The value of η is compatible with an estimate for an O(4) DQCP [45] and slightly below the SO(5) value [2, 12].

On the AFM side (Fig. 5d), $1/T_1$ is dominated by the 3D effects causing $T > 0$ AFM order, with the associated peak in $1/T_1$ masking any 2D quantum criticality, unlike the PS side, where the spin correlations and 3D effects are much weaker. We lack 2.4 GPa data above the tem-

peratures in Fig. 5c. At 2.1 GPa, no scaling is observed between T_N and T^* in Fig. 5b, where a sharp drop below T^* is immediately followed by strong precursors to AFM ordering.

Quantum spin model.— We now turn to the checkerboard J - Q model (CBJQM), in which four-spin interactions Q replace J' in the SSM. The CBJQM is amenable to quantum Monte Carlo simulations and hosts PS and AFM phases separated by a first-order transition with emergent O(4) symmetry at zero field [7]. We here simulate (Methods [33]) the same model in a field, defining $g = J/Q$ and $h = H/J$ with $J = 1$.

In the phase diagram in Fig. 6b, the field-driven PS–AFM transition is first-order. The PS gap $\Delta(h)$ obtained from the low-temperature susceptibility (SI, Sec. S8 [33]) is shown in Fig. 6c at $g = 0.2$, below the $h = 0$ transition at $g_c(0) \approx 0.217$. The expected linear form $\Delta(h) = \Delta(0) - h$ for an $S^z = 1$ excitation is observed for $h < h_c$, with h_c slightly less than $\Delta(0)$ implying a small gap discontinuity at h_c . We also observe (SI, Sec. S8 [33]) a very small magnetization jump, about 0.002 per spin. These behaviors are reminiscent of the well-known “spin-flop” transitions from Ising to canted XY AFM phases,

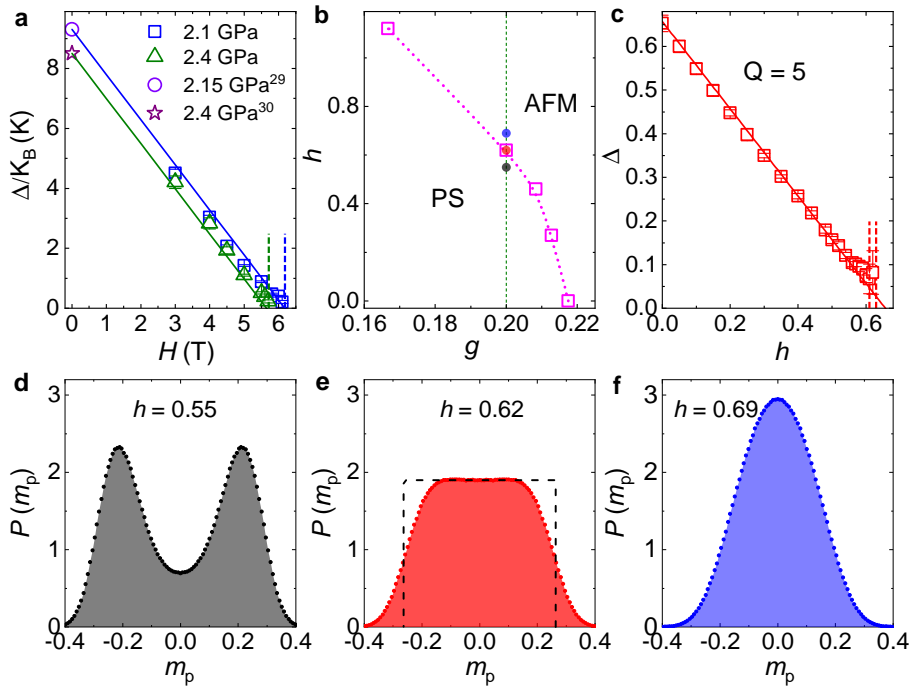


Figure 6. **Spin gap and emergent symmetry.** **a** Field dependent gap of $\text{SrCu}_2(\text{BO}_3)_2$. The lines show the expected form $\Delta(H) = \Delta(0) - \tilde{g}\mu_B H$ where $\Delta(0)$ are reported zero-field gaps [29, 30] and $\tilde{g} = 2.28$ is the known g -factor (SI, Sec. S5). The vertical dashed lines represent H_c values from Fig. 5f. **b** Ground-state phase diagram of the CBJQM vs $g = J/Q$ and field h . The PS and AFM phases are separated by a first-order transition. The vertical line and closely spaced points mark the parameters in panels **d-f**. **c** Spin gap of the CBJQM at $g = 0.2$. The dashed vertical line indicates h_c and the solid line is a fit to $\Delta(h) = \Delta(0) - h$. **d-f** Distribution of the plaquette order parameter. Double-peak (**d**), plateau (**e**), and single-peak (**f**) distributions are found respectively in the PS phase ($h = 0.55$), at the transition ($h = 0.62$), and in the AFM phase ($h = 0.69$).

but with anomalously small magnetization discontinuity. We argue in SI (Sec. S8 [33]) that the small magnetization and gap discontinuities, which decrease further upon moving closer to $g_c(0)$, reflect an approximate emergent $O(3)$ symmetry in the CBJQM at $h > 0$.

The emergent symmetry can also be studied directly. At $h = 0$, the $O(3)$ AFM order parameter (m_x, m_y, m_z) combines with the scalar PS order parameter m_p into an $O(4)$ vector (m_x, m_y, m_z, m_p) at the $T = 0$ transition [7, 43]. To detect the putative $O(3)$ symmetry of (m_x, m_y, m_p) at $h > 0$, we study the distribution $P(m_p)$ along the vertical line in Fig. 6b. In the PS phase, Fig. 6d, $P(m_p)$ exhibits the expected double peak, reflecting the Z_2 symmetry that is broken in the thermodynamic limit. In the AFM phase, Fig. 6f, there is a single central peak, reflecting the lack of PS order.

At a conventional first-order transition, a three-peak distribution would follow from coexisting PS and AFM orders. In contrast, the distribution in the coexistence state in Fig. 6e is nearly uniform over a range of m_p values (with finite-size rounded edges). The distribution $P(m_p)$ obtained by integrating an $O(3)$ symmetric $P(m_p, m_x, m_y)$ over m_x and m_y should indeed be uniform for $m_p \in [-R, R]$, where $R \equiv \max(|m_p|)$; thus the approximately flat distribution demonstrates emergent

$O(3)$ symmetry in the presence of finite-size fluctuations of R . Though this symmetry cannot be exact, i.e., it exists up to some finite length scale, it is responsible for suppressing T_c and the gap at H_c ; see further SI, Sec. S8 [33], where we also show supporting results for cross correlations between the PS and AFM order parameters.

We expect the same $O(3)$ emergent symmetry at the PS–AFM transition in $\text{SrCu}_2(\text{BO}_3)_2$, where the ordered coexistence state breaks the symmetry. The symmetry should be violated on long length scales, because of the distance to the DQCP and also by 3D couplings. One of the Goldstone modes associated with the coexistence state then develops a small gap. Studies of the CBJQM with inter-layer couplings suggest that the symmetry is surprisingly robust [43].

Emergent $O(3)$ symmetry on large length scales in $\text{SrCu}_2(\text{BO}_3)_2$ is supported, in particular, by our results at 2.1 GPa, where Fig. 4c shows a large discontinuity in the AFM order parameter but T_c is low and the gap (Fig. 6a) is very small at H_c . Moreover, the uniform magnetization is extremely small and does not exhibit a discernible discontinuity (SI, Sec. S4 [33]). These behaviors are analogous to those in the CBJQM for g close to $g_c(0)$.

Discussion.— Our high-pressure NMR experiments

on $\text{SrCu}_2(\text{BO}_3)_2$ in a magnetic field establish the first example of a quantum magnet realizing DQCP phenomenology, which so far existed only in the realm of field theories and model studies. We have demonstrated PS and AFM transitions with $T_P(H)$ and $T_N(H)$ merging at $T_c \simeq 0.07$ K and $H_c \simeq 6$ T. The PS–AFM transition at H_c is first-order, with discontinuity weakening with increasing pressure.

We have argued that the remarkable suppression of T_c and absence of significant PS gap discontinuity are consequences of emergent $O(3)$ symmetry generated by a nearby DQCP. At the highest pressure, 2.4 GPa, $1/T_1$ exhibits critical scaling for T between 0.2 and 2 K, indicating sufficient proximity to the DQCP (which is likely of the multi-critical type [14, 15, 17, 18]) for realizing the characteristic quantum-critical fan [46] on the gapped PS side of the transition. Strong 3D AFM ordering effects on the gapless side of the transition mask putative quantum-criticality in $1/T_1$ there, but the AFM ordering temperature T_N vanishes in a way very similar to the PS ordering T_P , again in support of emergent symmetry of the order parameters.

The $H = 0$ AFM phase was previously detected in the specific heat between 3.2 and 4 GPa [30], with T_N from 2 K to 3.5 K. Subsequently, results at $H > 0$ were also reported [31]. However, while $T_P(H)$ from the specific heat agrees well with our PS transitions in Fig. 1d, the heat capacity peak assumed to signal the AFM transition did not drop below 1 K [31], extending above the PS phase at fields as low as 3 T. It may be difficult to detect the small specific-heat peak signaling the AFM transition [30] in high-field measurements at low temperatures.

Beyond the highest pressure reached here, a plausible scenario [15, 17] is a QSL between the PS and AFM phases (Fig. 2). Our experiments do not directly address the putative QSL, and further investigations should elucidate the low- T , $H = 0$ state between 2.6 and 3 GPa

(where no order has been detected [30, 31]) and its evolution as H approaches 5.7 T, where our current experiments point to a DQCP slightly above 2.4 GPa.

Acknowledgments.— We would like to thank Bruce Normand for his extensive suggestions and constructive criticism. We also thank Wenan Guo, Frédéric Mila, Masashi Takigawa, Yiming Wang, Zhi-Yuan Xie, and Yi-Zhuang You for helpful discussions. This work was supported by the National Natural Science Foundation of China under Grants No. 12134020, 12104503, 12174441, 51872328, and 11874401, the Ministry of Science and Technology of China under Grants No. 2016YFA0300504 and 2017YFA0302903, the Simons Foundation under Simons Investigator Grant No. 511064, the China Postdoctoral Science Foundation under Grant No. 2020M680797, Beijing Institute of Technology Research Fund Program for Young Scholars, and the Fundamental Research Funds for the Central Universities and the Research Funds of Renmin University of China under Grants No. 21XNLG18 and 18XNLG24. Some of the numerical calculations were carried out on the Shared Computing Cluster managed by Boston University’s Research Computing Services.

Author contributions.— Y.C. performed NMR measurements and data analysis with assistance from C.L., Z.H., and W.Y.. W.H. and S.L. provided single crystals. X.L. and H.L. performed the Bayesian fitting analysis. L.L., H.L., N.X., and K.H.W. performed numerical simulations with guidance from R.Y. and A.W.S.. W.Y., A.W.S., and R.Y. guided the project and wrote the manuscript with input from all the authors.

Competing interests.— The authors declare that they have no competing interests.

Data and materials availability.— All data needed to evaluate the conclusions in the paper are present in the manuscript or the Supplementary Materials.

Supplemental Information

Proximate deconfined quantum critical point in $\text{SrCu}_2(\text{BO}_3)_2$

Yi Cui, Lu Liu, Huihang Lin, Kai-Hsin Wu, Wenshan Hong, Xuefei Liu, Cong Li, Ze Hu, Ning Xi, Shiliang Li, Rong Yu, Anders W. Sandvik, and Weiqiang Yu

S1. METHODS**A. Experiments**

Single crystals of $\text{SrCu}_2(\text{BO}_3)_2$ were grown by the floating-zone method. We used a NiCrAl piston cell for the high-pressure NMR measurements and Daphne 7373 oil as the pressure medium. The pressure was calibrated using the low-temperature Cu_2O NQR frequency [47], and the highest pressure achieved was 2.4 GPa. NMR experiments were performed in two types of cryostat: a variable-temperature insert (VTI) was used for measurements in the temperature range from 1.5 K to 50 K and a dilution refrigerator was used to achieve temperatures ranging from 0.07 K to 2 K.

B. NMR spectrum

The ^{11}B spectra were obtained by the standard spin-echo technique. ^{11}B nuclei have spin $I = 3/2$, whence the NMR spectra and line widths contain contributions from both local magnetism and electric-field gradients (EFGs). The local Hamiltonian for a nucleus with spin I and quadrupole moment Q can be described by the following form,

$$\mathcal{H}_n = \mathbf{I} \cdot \mathbf{B} + \sum_i A_{\text{hf}}^{\alpha\beta}(i) I^\alpha S_i^\beta + \frac{e^2 q Q}{4I(2I-1)} [3I_z^2 - \mathbf{I}^2 + \eta(I_x^2 - I_y^2)], \quad (\text{S1})$$

where the three terms describe, respectively, the coupling of the nuclear spin to the external field, the hyperfine coupling between the nuclear spin and neighboring electronic spins, and the coupling between the nuclear quadrupole moment and the local EFG. The factor q in the last term is from the EFG tensor (the component along the principal axis), which is produced by the local electronic structure of the ions.

To identify the ordered phases and clarify their nature, NMR spectra were measured over a wide field range from $H = 0.2$ T to 15 T along the crystalline c axis, with a top-tuning circuit allowing for the corresponding wide range of frequencies. The full spectrum was obtained by the frequency-sweep method, which covers one center line and two sets of satellites on each side of it. Figure 3a of the main text shows a typical NMR spectrum at 4 T. It contains one center line, with a frequency of

approximately zero relative to $^{11}\gamma H$, where $^{11}\gamma$ is the Zeeman factor, and two sets of satellites aligned from ± 1.0 MHz to ± 1.4 MHz. We define the Knight shift as $^{11}K_n = f/^{11}\gamma H - 1$, where f is the position of the center peak in the spectrum.

The NMR magnetic field was oriented primarily along the c axis, with a 8.6° tilting applied to separate the four ^{11}B sites producing satellites in the spectrum. The angle is calibrated by different satellite frequencies ν_Q of four sets of satellites shown in Fig. 3a, as reported by the earlier NMR study [35]. The four satellites arise because each ^{11}B site has a different orientation of the principal EFG axis relative to the (tilted) external field. Each satellite line cannot be assigned to a specific ^{11}B site because we did not characterize the exact direction of the field in the sample ab plane.

C. NMR line widths

For a system with local inhomogeneity, the FWHM of the NMR center line has two additive terms, the hyperfine field contribution, which scales linearly with the applied field, and a second-order EFG correction, which is weak and scales inversely with the field. In a field of 0.2 T and at temperatures below 5 K, the FWHM of the center line is of order 2 kHz. By contrast, although the FWHM of the satellites has a similar hyperfine-field contribution, it has a large and nearly field-independent first-order EFG contribution, making the FWHM of each satellite larger than 10 kHz for the same temperature range and field.

D. NMR spin-lattice relaxation rate

The relaxation time $^{11}T_1$ was measured using the spin-inversion method by applying a π inversion pulse (of duration 4 μs). In all phases displaying a line-splitting, the $1/^{11}T_1$ data reported in the main text were measured on the higher-frequency peaks, meaning f_R in Fig. 4a, although $1/^{11}T_1$ measured on f_L was verified to be consistent in every case with that on f_R .

Note that $1/^{11}T_1$ overall increases with the field, as shown Fig. 5 of the main text. In particular, this increase follows the expectations in the quantum-critical fan on the PS side of the transition, analyzed in Fig. 5e. This behavior indicates dominant contributions from the hyperfine field fluctuations originating from the critical

spin fluctuations. By contrast, the EFG contributions, which are caused indirectly by bond and plaquette singlet fluctuations that couple to the lattice [causing fluctuations of q in Eq. (S1)], are expected to decrease with the field because the PS fluctuations are suppressed by the field.

The most likely reason for the absence of visible EFG contributions in the $1/^{11}\text{T}_1$ data is that the singlet fluctuations in the frustrated magnet induce bond-length fluctuations of relatively small amplitude, i.e., the fluctuations of q in Eq. (S1) are small and generate insignificant contributions to $1/T_1$ compared to the spin fluctuations mediated directly through the hyperfine coupling.

Evidence for different scales of the effective EFG and hyperfine couplings come from the way we have detected the PS and AFM order parameters using the NMR line shape. In the case of PS order, in Fig. 3b of the main text we used the FWHM of the central and satellite lines, because the expected peak splitting is too small to observe. Thus, the lattice deformation induced by the frozen singlets, i.e., the modulation of q in Eq. (S1), is very small. In contrast, the peak splitting is very substantial in the AFM phase, Fig. 4. Given the small modulation of q in the ordered PS state, the fluctuations of q above and close to the PS transition temperature, induced indirectly by quantum fluctuations of bond and plaquette singlets, should also be small and contribute insignificantly to $1/T_1$ compared to the spin fluctuations mediated directly by the large coupling A_{hf} . We are therefore justified in analyzing $1/T_1$ solely in terms of spin fluctuations detected through the hyperfine coupling—this assumption is often made in NMR studies of quantum magnets without the supporting evidence we have here from the weak response in the PS state.

It is also possible, in principle, that $1/^{11}\text{T}_1$, as an anisotropic probe of EFG and magnetic fluctuations, may not significantly sense the anisotropic EFG fluctuations geometrically by accident [48]. Because of our direct evidence of insignificant EFG contributions due to the small amplitude of the lattice fluctuations, there is no need to invoke such a mechanism here, however.

E. Fitting using Bayesian inference

To obtain the fitting parameters for the functional forms of $T_{\text{N}}(H)$ and $T_{\text{P}}(H)$, with these phase boundaries coming together at a low common T_c value at $H = H_c$, we followed the Bayesian inference procedure of Ref. [49]. Sets of points spanning the multidimensional parameter space are generated by a Markov-chain Monte Carlo process and the output is a statistical model for the probability that a given parameter set can describe the measured data. The errors inherent to the data are then reflected systematically as the uncertainties in each of the fitting parameters. For further details we refer to Ref. [49].

The functional forms used to model the transition temperatures are given in the main text and the maximum-

probability results for pressures 2.1 and 2.4 GPa are shown in Fig. 5f. Probability distributions for the system parameters consistent with the measured data are shown in Sec. S6 of the SI, and these distributions underlie the error bars on the parameters reported in the main text.

F. QMC simulations of spin models

The Hamiltonian of the CBJQM, i.e., the J - Q model [2] defined on the checkerboard lattice [7], subject to an applied magnetic field is given by

$$\mathcal{H} = -J \sum_{\langle ij \rangle} P_{ij} - Q \sum_{ijkl \in \square_s} (P_{ij} P_{kl} + P_{ik} P_{jl}) - H \sum_i S_i^z, \quad (\text{S2})$$

where \mathbf{S}_i is an $S = 1/2$ spin operator at site i and $J > 0$ is the nearest-neighbor AFM Heisenberg coupling, with the corresponding operator defined for convenience as a singlet projector,

$$P_{ij} = 1/4 - \mathbf{S}_i \cdot \mathbf{S}_j. \quad (\text{S3})$$

The second term describes a partial ring-exchange-type interaction (or correlated singlet projection) defined on plaquettes \square_s with a checkerboard arrangement on the square lattice. The third term describes the external magnetic field of strength H .

For the simulation results shown in Figs. 6b-6f of the main text, we took $J = 1$ as the unit of energy to define the dimensionless parameter $g = J/Q$ and the reduced field $h = H/J$. We studied this model by stochastic series expansion (SSE) quantum Monte Carlo (QMC) simulations [50] on systems of sizes $L \times L$ up to a maximum of $L = 64$ and down to a minimum temperature of $T = J/L$. The SSE method is exact, in the sense that it is based on a construction corresponding to a complete representation of the imaginary-time dimension of a quantum system when mapped into a classical model (on which the Monte Carlo sampling is performed), and thus the simulation results are only affected by statistical errors.

To characterize the PS-AFM transition (Sec. S8 A and S8 B), we used an order parameter for the PS phase of the form

$$m_p = \frac{2}{L^2} \sum_{\mathbf{i} \in \square_s} (-1)^{i_x} S^z(\mathbf{i}) S^z(\mathbf{i} + \hat{x}) S^z(\mathbf{i} + \hat{y}) S^z(\mathbf{i} + \hat{x} + \hat{y}), \quad (\text{S4})$$

where \mathbf{i} is the position vector of the checkerboard plaquettes and i_x denotes the row index of \mathbf{i} . We also calculated the uniform magnetic susceptibility,

$$\chi = \frac{\partial m}{\partial h}, \quad m = \frac{1}{N} \sum_{i=1}^N \langle S_i^z \rangle, \quad (\text{S5})$$

where $N = L^2$. In the simulations we obtained the susceptibility in the standard way from the magnetization

fluctuations,

$$\chi = \frac{N}{T} [\langle m^2 \rangle - \langle m \rangle^2], \quad (\text{S6})$$

where $\langle m \rangle = 0$ in the absence of external field. We extracted the spin excitation gap in the PS phase by fitting our numerical results to the form $\chi(T) \propto e^{-\Delta/T}$ at low temperatures for each field.

In addition to the above observables, which can be obtained using diagonal estimators in the S^z basis used, we also study cross-correlations between the AFM and PS order parameters. In the case of $h = 0$, we can use the diagonal correlator $\langle m_z^2 m_p^2 \rangle$, where m_z is z -component of the staggered magnetization, but when $h > 0$ the magnetization operator in $\langle m_x^2 m_p^2 \rangle = \langle m_y^2 m_p^2 \rangle$ is off-diagonal and a more complicated estimator based on the directed-loop SSE updates is required. Essentially, in the directed-loop updates used to evolve the configurations [50], the probability distribution of the two open ends of a uncompleted loop (i.e., a string) at the construction stage is related to the off-diagonal operator $m_x^2 + m_y^2$ (here in the case where the string ends are located at the same ‘‘time slice’’ in the SSE operator space). We follow the implementation discussed by Dorneich and Troyer [51], with the modification that each contribution is also multiplied by the diagonal operator m_p^2 when accumulating the cross-correlation function $\langle (m_x^2 + m_y^2) m_p^2 \rangle$.

To complement the simulations of the CBJQM, we also apply SSE QMC simulations to study an anisotropic XXZ Heisenberg $S = 1/2$ spin model given by the Hamiltonian

$$\mathcal{H} = -J \sum_{\langle ij \rangle} (P_{ij} - \lambda S_i^z S_j^z) - H \sum_i S_i^z, \quad (\text{S7})$$

where λ expresses the spin anisotropy as a deviation from the Heisenberg model.

The XXZ model clearly has an exact $O(3)$ symmetry at $\lambda = 0$, while perturbations with $\lambda < 0$ imply an $O(2)$ and with $\lambda > 0$ a Z_2 (Ising) order parameter. For $\lambda > 0$, the system undergoes a first-order ‘‘spin-flop’’ transition versus the magnetic field; for small h remaining in the Ising phase and transitioning through a level crossing into a canted XY (planar) AFM. We use this transition as a well understood benchmark case for comparing and contrasting with the CBJQM results in Sec. S8 of the SI.

S2. INEQUIVALENT BORON SITES IN THE PS PHASE

The planar lattice structure of $\text{SrCu}_2(\text{BO}_3)_2$ is shown in Fig. 1a of the main text, and is represented in a more detailed way in Fig. S1 to illustrate the singlet formation in the full-plaquette (FP) variant of the PS state. Each unit cell contains four B sites, B1 to B4, which are equivalent in the DS state at zero field. For applied fields with an in-plane component, these four sites become inequivalent by field orientation with respect to the

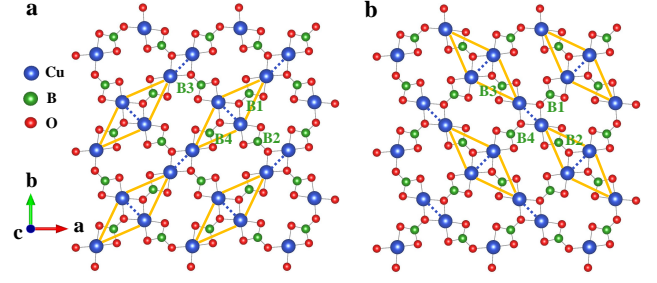


Figure S1. Illustration of the FP phases in one planar layer of $\text{SrCu}_2(\text{BO}_3)_2$, where each singlet forms on the yellow diamond composed of four Cu ions, which includes one Cu dimer (short dashed lines). B1 to B4 label the four B sites in each unit cell of $\text{SrCu}_2(\text{BO}_3)_2$, which are inequivalent in a magnetic field tilted away from the c -axis. **a** and **b** represent the two degenerate FP states, in each of which only one type of diamond (dimer) orientation is selected.

B-O bond directions. The NMR spectrum of ^{11}B consists of one center line and two satellite lines (Fig. 3a of the main text); the satellite frequencies are affected by both the hyperfine field and a first-order correction from the EFG, whereas the center line is affected by the hyperfine field and a weaker second-order EFG correction (which is negligible at fields above 2 T).

When the applied field is tilted away from the c axis, failure to discern four peaks in the center line at low fields simply indicates that the difference in hyperfine effects on the four sites is too small to be resolved. By contrast, the four distinguishable satellite peaks shown in Fig. S2a are a clear indication for strongly differing EFG effects (i.e. principal axes of the local EFG) at sites B1 to B4.

Recent studies of the SSM find a close energetic competition between the two possible plaquette states [11, 39]; the FP state in which a dimer is enclosed in the local four-spin singlet (represented in Fig. 1b of the main text) and the empty-plaquette (EP) phase in which no dimer is enclosed. The double degeneracy of the FP phase is shown explicitly for the planar lattice structure of $\text{SrCu}_2(\text{BO}_3)_2$ in Figs. S1a and S1b; the two diamond (dimer) directions are mutually orthogonal. Because of the shape of the four-spin units involved in the spontaneous breaking of the two-fold symmetry when the FP state forms, this phase transition must be accompanied by an orthorhombic distortion of the lattice. In a bulk single crystal, when the plaquette phase is entered on cooling, the degeneracy associated with the distortion in the FP phase is expected to lead to structurally twinned domains, i.e., macroscopic coexistence of the degenerate ground states by phase separation.

Figure S2 shows NMR satellite spectra measured through the FP PS transition in both conventional and dilution refrigerators, under very low field to reduce the magnetic broadening of the line. Each line has a Lorentzian shape, a result we used to fit their FWHM, which is displayed in Fig. 3b of the main text. The strong

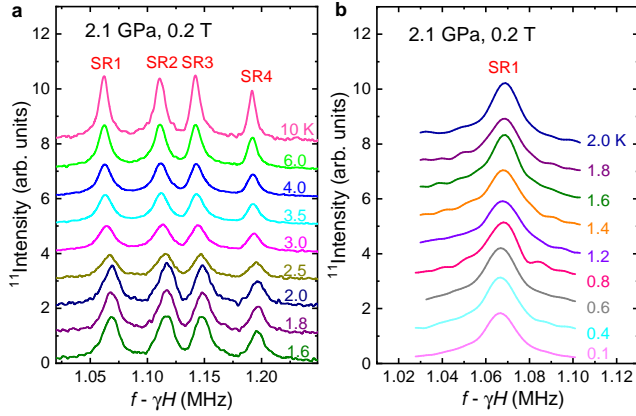


Figure S2. **a** High-frequency NMR satellite spectra measured in a conventional He refrigerator under a pressure of 2.1 GPa and a small field of 0.2 T. SR1-SR4 are associated with the four B sites, as labelled in Fig. S1, although the precise B site corresponding to each NMR line is not determined. **b** Satellite SR1 measured in the dilution refrigerator at 2.1 GPa and 0.2 T.

change of FWHM observed below 1.8 K in the NMR satellite, but not in the center line, is understood from local lattice distortions as follows: The twinning of the FP phase leaves any given B site (e.g. B1) either inside (Fig. S1a) or outside (Fig. S1b) the local diamond-shaped FP [35]. This leads to a splitting of the ^{11}B spectra, because the different B1 sites have different hyperfine fields and local EFGs. The nuclear quadrupole moment on the inside site experiences a larger EFG due to the lattice contraction, and conversely for the outside site, causing a further splitting of each satellite.

The large increase observed in the FWHM of the satellites below 1.8 K in Fig. 3b of the main text is consistent with such an EFG effect, which is too small to be resolved as a line splitting but is responsible for the order parameter behavior of the FWHM. The much weaker increase in the FWHM of the center line excludes a dominant role for magnetic effects on the NMR line shapes at such a low field, meaning that the explanation requires local structural distortions.

In contrast to the two inequivalent sites forming in the FP state, in an EP state all the B sites reside outside the square plaquettes and experience a reduced EFG, whence a narrowing of the FWHM would be expected. Thus, we have confirmed that the PS state is of FP type, where the lattice has undergone an orthogonal distortion [39].

S3. NMR KNIGHT SHIFT AND $1/T_1$ AROUND THE DS-PS PHASE TRANSITION

Figure 3c in the main text shows the evolution of the NMR center line (arrows) for several temperatures at pressure 0.9 GPa and field 4 T. The spectrum has a single peak with a negative Knight shift for tempera-

tures from 10 K to 2 K, consistent with the negative hyperfine coupling, $A_{\text{hf}} \simeq -0.259 \text{ T}/\mu_{\text{B}}$, for $\vec{H} \parallel \hat{c}$ [34, 35]. The change of the ^{11}B NMR Knight shift, $^{11}K_n(T)$, is shown in Fig. S3a for two low field values and a wide range of pressures. The saturation of $^{11}K_n$ below 2 K to approximately 0.05% that is observed at all pressures is caused by a temperature-independent orbital contribution, $^{11}K_{\text{orb}}$, as a result of which the magnetic contribution to the hyperfine coupling is then taken as $^{11}K_s(T) = ^{11}K_n(T) - ^{11}K_{\text{orb}}$. Similarly, $^{11}K_n$ at all pressures decreases slowly when cooled down to 10 K from high temperatures (data not shown), consistent with PM behavior given the negative hyperfine coupling.

Returning to the interpretation of Fig. 3c, the change of $^{11}K_n(T)$ is smooth for pressures below 1.85 GPa, matching the rapid drop of the susceptibility as the temperature decreased below the spin gap of the DS state, and consistent with a crossover but no phase transition (only an increasing density of singlets on the J' bonds as T is lowered). Figure S3b shows the analogous behavior in spin-lattice relaxation rate, $1/^{11}T_1$, for the same pressures and fields.

By contrast, for pressures at and above 1.85 GPa Fig. S3 shows more sudden drops of $^{11}K_n$ and $1/^{11}T_1$ on cooling through an onset temperature that we label as T^* . The reduction of the uniform susceptibility and the low-energy spin fluctuations here indicate either a sharp crossover or a true phase transition into the PS liquid phase (where plaquette singlets form but do not yet order) identified in the main text.

To distinguish between a phase transition and a sharp cross-over, Figs. 3d in the main text is helpful. It again shows the center NMR line at a series of temperatures, in this case at 1.85 GPa and 4 T. Above 4 K, the spectrum has a single peak with a negative Knight shift. The Knight shift again increases rapidly on cooling, and in this case a line splitting is observed below 4 K with two peaks labeled as f_1 and f_2 respectively. The spectral weight of the f_1 peak first increases on cooling below 4 K but then vanishes at 2.9 K. This line splitting is observed only at 1.85 and 1.95 GPa.

The appearance of two lines over a finite temperature range suggests the phase coexistence expected when the system crosses the first-order transition between the DS and PS liquid phases, i.e., at temperatures below the critical point where this line of transitions terminates, as indicated schematically in Fig. 2a of the main text. Given that the system at 1.85 GPa is in the PS phase at low temperatures, the f_1 peak, which is gradually suppressed below 4 K and is absent below 2.9 K, must be associated with the DS phase. The f_2 peak, which remains as a single peak below 2.9 K, corresponds to another phase. Because of its spectral character, discussed below (see also Sec. S2), we identify it as arising from regions in the PS liquid phase.

Thus the line splitting is the signal that the process occurring around 4 K at 1.85 and 1.95 GPa is a genuine first-order magnetic transition from the PM phase

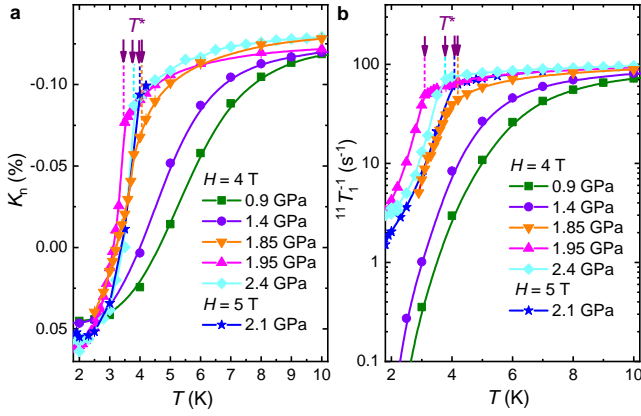


Figure S3. **a** Knight shift, $^{11}K_n(T)$, shown for a number of different pressures and fields. **b** Spin-lattice relaxation rate, $1/^{11}T_1(T)$, shown for the same pressures and fields. In both panels, T^* indicates the temperature below which a dramatic change is observed in $^{11}K_n$ and $1/^{11}T_1$. Here $^{11}K_n$ and $1/^{11}T_1$ for pressures at and above 1.85 GPa were measured on the f_2 peak shown in Fig. 3 of the main text.

into the PS liquid. This is possible when the first-order DS transition line is not vertical in the (P, T) plane, but has a finite slope toward higher pressures as T increases, as represented in Fig. 2a of the main text. Within the uncertainties of pressure calibration in different specific-heat measurements, this is consistent with the identification of the DS–PS transition between 1.7 and 1.8 GPa at temperatures below 2 K in Ref. [30], while the Ising-type critical point was located at 3.3 K and approximately 1.9 GPa in Ref. [31].

It should be noted that both phases are of singlet type and therefore the first-order line is not sensitive to the magnetic field strength even at the rather high fields, 4 and 5 T, used in Figs. 3c–e. Phase coexistence over a rather wider range of temperatures, 3 ~ 4 K, is explained by a very mild slanting of the transition line in the region where this line is crossed. Thus, the system remains very close to the transition line for an extended range of temperatures.

The highest pressure at which we have observed this line splitting is 1.95 GPa, indicating that phase coexistence is terminated there, in good agreement with $P \simeq 1.9$ GPa for the critical end point determined from the heat capacity in Ref. [31]. Certainly no line splitting is observed at 2.1 GPa in Fig. 3e of the main text. This is in contrast to Ref. [35], where a different line splitting was observed at 2.4 GPa [35].

Previous NMR works at 2.4 GPa reported two types of line splitting, with one occurring below 30 K, and one below 4 K with a large line split of ~ 0.2 MHz [35, 36]. These line splitting are different from our observation with a much smaller line split (~ 0.03 MHz), at lower pressures. The previous reported line splits may be caused uniaxial pressure inhomogeneity which is enhanced upon cooling and breaks the tetragonal crystal symmetry. Our sample

resolves clearly the PS and the AFM phases and their respective transition temperatures, indicative of high sample quality and pressure homogeneity. Therefore, it is unlikely that disorder effects are significant in our sample and smears out other orderings, in contrast to a doped Han purple compound [49].

Above the small pressure window 1.85 ~ 1.95 GPa, the single center peak with its very rapid change in K_n and $1/T_1$ at 3 ~ 4 K persists at all higher pressure measurements in Fig. S3. Because the change from the high- T PM phase to the PS liquid phase should not be a true phase transition when the pressure is sufficiently high or low for the first-order DS line to be avoided, we conclude that T^* for $P > 1.95$ GPa reflects an extremely sharp crossover. We stress that, in the PS liquid, the plaquette singlets fluctuate between the two orthogonally directed local plaquette types, so that no local symmetry-breaking occurs in this phase, only in the ordered PS state below 2 K. The cross-over is manifestly very sharp close to the Ising-type critical point, as reflected also in the sharp peaks in the specific heat [30, 31]. Thus, the NMR signal can easily be mistaken for a true phase transition, which would not be compatible with the critical-point scenario and other aspects of the phase diagram.

Though all of our observations at 3 ~ 4 K are consistent with the critical-point scenario [31] and sharp crossovers at T^* from the PM phase, we still offer an alternative scenario for completeness: The critical Ising point scenario was considered theoretically from the perspective of a 2D system [31], but in principle 3D effects could turn the critical point into a triple point (with large fluctuations since the 3D couplings should be very weak); the nexus of three first-order transitions. Then, the PM phase (which can be interpreted as a gas phase) would turn upon lowering the temperature into either the PS liquid or the DS phase (which then also should be considered as another liquid-like phase) through a very weak first-order transition without any symmetry breaking. This alternative scenario, for which we do not have any evidence, experimental or theoretical, would not affect the other parts of the phase diagram in Fig. 2, including the DQCP scenario.

S4. AFM SPECTRA AND PHASE TRANSITIONS

A. Continuous temperature-driven transition

In Fig. 4a and 4b of the main text we showed the splitting of the NMR center line as the system is driven from the PS to the AFM phase by increasing the applied field. The two field-induced peaks are located symmetrically around the zero of frequency measured relative to $f_0 = ^{11}\gamma H$. This symmetrical line splitting indicates the onset of equal negative and positive hyperfine fields and constitutes direct evidence for AFM ordering. To complement the results for the field-driven PS–AFM transi-

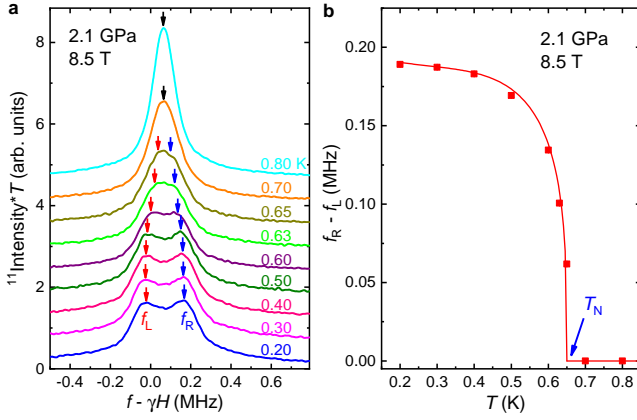


Figure S4. **a** NMR spectra measured over a sequence of dilution-refrigerator temperatures at $P = 2.1$ GPa and $H = 8.5$ T. The data sets are offset vertically for clarity. Black arrows mark the single-peak locations while the red and blue arrows mark the locations of the split peaks, at the respective frequencies f_L and f_R determined by the double-Lorentz fitting, that signal the AFM phase. **b** Peak-splitting $f_R - f_L$ (a proxy AFM order parameter) shown as a function of temperature. T_N marks the transition temperature into the AFM phase, where $f_R - f_L$ rises from zero. The fitted curve has the asymptotic form $f_R - f_L \propto (T_N - T)^\beta$ with $T_N = 0.65$ K and $\beta = 0.305$.

tion, here we discuss the line splitting observed at constant field as a function of the temperature. The center line of the NMR spectrum at 2.1 GPa and 8.5 T is shown in Fig. S4a over a range of low temperatures. A single line is observed at and above 0.7 K, but below 0.65 K the spectrum shows two peaks, labeled as f_L and f_R .

We again use the frequency difference $f_R - f_L$ as a proxy for the AFM order parameter, which we show as a function of temperature in Fig. S4b. We observe that $f_R - f_L$ rises rapidly on cooling below T_N , and note that for this field, $1/^{11}\text{T}_1$ displays a clear peak at the same temperature, as shown in Fig. 5b of the main text.

Because no obvious three-peak signature of phase separation can be observed in the NMR spectra in Fig. S4a, our results in this case establish a continuous or very weakly first-order AFM transition on cooling in a constant field 8.5 T, which is significantly away from the common transition field $H_c \approx 6.2$ T. Close to the first-order triple point that we have established in the main text at (T_c, H_c) and 2.1 GPa, the transition should remain first-order, while sufficiently far away from the triple point one should expect continuous transitions (as has been observed in model studies [43]).

The curve fitted to the data points in Fig. S4b is of the form $f_R - f_L = F(T_N - T)(T_N - T)^\beta$, where $F(x)$ is a second-order polynomial in $x = T_N - T$ to account for the cross-over from the asymptotic critical form to almost temperature independent at lower T . We do not have enough data for such a fit to produce quantitatively conclusive results, e.g., to rigorously test the exponent $\beta \approx 0.35$ corresponding to the expected 3D XY univer-

sality class for the $T > 0$ XY AFM transition. Nevertheless the behavior is consistent with a continuous or a very weakly first-order transition, and the exponent $\beta \approx 0.30$ obtained from the fit is reasonably close to the expected value.

We do not have enough $f_R - f_L$ data at other fields to systematically study the change from first-order to continuous AFM transitions as the field strength is varied. Similar to the situation at 2.1 GPa, splitting of the center NMR line is also observed at 1.95 and 2.4 GPa in the same range of temperature.

Technically, because the ^{11}B sites are located slightly above the Cu plane and have dipolar coupling to the Cu moment [35], establishing in-plane AFM moments on the Cu sites ought to produce a dipolar hyperfine field along the c axis at the ^{11}B sites, which due to the AFM order is antiparallel on different sites. Our results are then consistent with the expected planar rather than c -axis AFM order, because the latter would produce a much larger uniform c -axis magnetization, which, as we discuss below in Sec. S4D, is not observed at such low fields.

B. First-order field-driven transition

The low-temperature ^{11}B NMR spectra at 2.1 GPa and 2.4 GPa and at 0.07 K, presented in Fig. 4a and 4b of the main text, show that the field-induced AFM ordering is accompanied by a narrow regime of magnetic fields exhibiting phase coexistence around the AFM transition detected at our lowest temperature of 0.07 K.

As shown in Fig. 4a, at 2.1 GPa, a significant line splitting is detected all the way down to the field H_c determined from the fits illustrated in Fig. 5f, demonstrating that the transition is rather strongly first-order in this case. In contrast, at 2.4 GPa, the line cannot be reliably separated into three different peaks below 5.8 T, which is still some distance away from the transition field $H_c = 5.72$ T. Thus, while the transition is also first-order at this higher pressure, the discontinuity has weakened significantly relative to that at 2.1 GPa, indicating that the system is approaching a continuous QCP (which we argue is a DQCP) located at only slightly higher pressure. The transition field also clearly moves down with increasing pressure, and the trends observed here suggest that H_c at the DQCP should be below 5.7 T.

C. Orientation of ordered moments

Because the hyperfine coupling between the ^{11}B nuclear spins and the Cu moments in $\text{SrCu}_2(\text{BO}_3)_2$ is dominated by dipolar interactions for the off-diagonal tensor elements of the hyperfine coupling [52], the hyperfine field at each ^{11}B nucleus can be estimated in the AFM state for different ordered configurations of the local moments. In general, the hyperfine field, $\mathbf{H}_{\text{in}} = (H_{\text{in}}^x, H_{\text{in}}^y, H_{\text{in}}^z)$, on a ^{11}B nucleus due to one neighboring Cu spin can be

| (a) [100] | | | |
|-----------|-------------------|-------------------|-------------------|
| site | H_{in}^x | H_{in}^y | H_{in}^z |
| B1 | -0.011 | -0.608 | -0.168 |
| B2 | 0.011 | -0.608 | 0.168 |
| B3 | 0.011 | -0.608 | -0.168 |
| B4 | -0.011 | -0.608 | 0.168 |

| (b) [010] | | | |
|-----------|-------------------|-------------------|-------------------|
| site | H_{in}^x | H_{in}^y | H_{in}^z |
| B1 | -0.608 | -0.011 | -0.168 |
| B2 | -0.608 | 0.011 | -0.168 |
| B3 | -0.608 | 0.011 | 0.168 |
| B4 | -0.608 | -0.011 | 0.168 |

| (c) [110] | | | |
|-----------|-------------------|-------------------|-------------------|
| site | H_{in}^x | H_{in}^y | H_{in}^z |
| B1 | -0.619 | -0.619 | -0.336 |
| B2 | -0.597 | -0.597 | 0 |
| B3 | -0.597 | -0.597 | 0 |
| B4 | -0.619 | -0.619 | 0.336 |

Table S1. Hyperfine fields at the ^{11}B nucleus for a system in which the AFM moments on the Cu^{2+} ions are oriented along the crystalline [100] (a), [010] (b), and [110] (c) directions. The field strengths are given in arbitrary units.

written as

$$\mathbf{H}_{\text{in}} = \tilde{\mathbf{A}}\mathbf{m}, \quad (\text{S8})$$

where $\mathbf{m} = (m^x, m^y, m^z)$ is the local moment of the Cu ion and the hyperfine coupling tensor has the form

$$\tilde{\mathbf{A}} = \begin{bmatrix} A^{aa} & A^{ab} & A^{ac} \\ A^{ba} & A^{bb} & A^{bc} \\ A^{ca} & A^{cb} & A^{cc} \end{bmatrix}. \quad (\text{S9})$$

All of the tensor elements can be estimated by using the general form of the dipolar field, with the relative positions of the ^{11}B nucleus and the Cu ion as input.

In the AFM phase induced by a field applied along the c axis, the Cu moments, which have strong Heisenberg interactions, should orient in the crystalline ab plane. The AFM order is collinear type, with parallel moments on each Cu dimer being antiparallel to those on all four neighboring dimers (Fig. 1c of the main text). If one assumes that the Cu moments are oriented along the [100] direction, the hyperfine fields at the four ^{11}B nuclei shown in Fig. S1 can be calculated by summing the contributions from all of the neighboring Cu sites, giving the result shown in Table S1(a). We note that the real hyperfine field in a material is usually enhanced by various factors beyond the simple dipolar-field calculation, but this approximation is sufficient for the qualitative conclusions we will draw. If one assumes that the Cu moments are ordered along the [010] or [110] directions, the resulting hyperfine fields at the four ^{11}B sites are those shown respectively in Tables S1(b) and S1(c).

These calculations show that H_{in}^z has one pair of negative and one pair of positive values for the four B sites

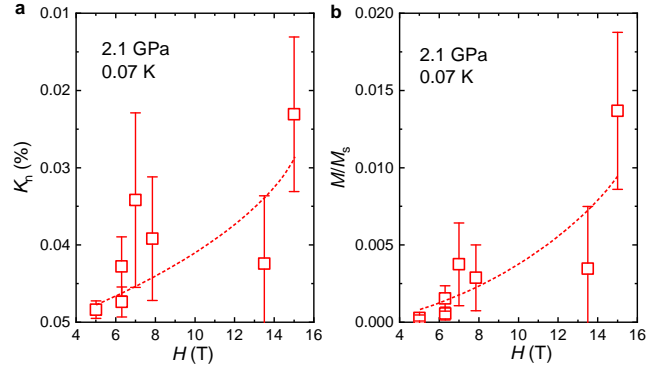


Figure S5. **a** Knight shift, $^{11}K_n$, calculated from the average frequency of the full NMR spectra presented in Fig. 4a of the main text and shown as a function of field at 2.1 GPa. The dashed line is a guide to the eye. **b** Uniform magnetization of the system, obtained from the Knight shift by averaging the frequency of the NMR lines.

when the AFM moments are oriented along the [100] or [010] directions. Such a pattern of hyperfine field components create a double NMR line splitting, which is consistent with our experimental observations (Fig. S4). By contrast, moments aligned in the [110] direction will split the NMR line into three, which is not consistent with our observations. Similarly, moments oriented in other directions, which are necessarily of lower symmetry, will also create three or more split NMR lines. Thus we conclude that the ordered moment in the field-induced AFM phase is aligned in the [100] or the [010] direction. Note that the small non-zero angle of the sample alignment in the field was not taken account in the calculations.

Because the hyperfine field components $H_{\text{in}}^{x,y}$ are not zero for planar AFM moment orientations (Table S1), the spin-lattice relaxation rate $1/^{11}T_1$, measured with $H \parallel c$, should pick up transverse fluctuations from the AFM phase. This is demonstrated by the peaks appearing in $1/^{11}T_1$ at the transition temperature, T_N , in Figs. 5b and 5d of the main text.

D. Knight shift and uniform magnetization

To further explore the nature of the AFM phase, we calculated the uniform magnetization, $M(H)$, at different applied fields from the NMR Knight shift. $^{11}K_n$ for the AFM phase is calculated from the average frequency, f , of the center line of each spectrum and the uniform magnetization is obtained from its magnetic part, K_s , using the expression $M = ^{11}K_s H / ^{11}A_{\text{hf}}$. For a pressure of 2.1 GPa, $^{11}K_n$ at our base temperature of 0.07 K is shown as a function of field in Fig. S5a. The resulting $M(H)$ is shown normalized to its saturation value, M_s , in Fig. S5b, for which we used a g -factor of $g_c = 2.28$ [53].

With $\vec{H} \parallel \hat{c}$, we find that the uniform magnetization never exceeds 2% of its saturation value at 15 T. Such

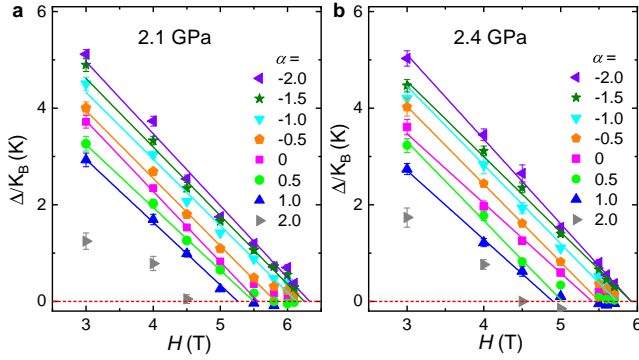


Figure S6. Spin excitation gaps obtained by fitting $1/T_1$ to the form Eq. (S10) with a series of values of α , plotted as functions of the field at pressure 2.1 GPa in panel **a** and 2.4 GPa in panel **b**. The straight lines correspond to the fitted form $\Delta/K_B = g(H_0 - H)$ with fitting parameters g and H_0 .

a high field is about 9 T above H_c , and therefore offers an energy scale of 14 K to partially polarize the system. This energy scale is not very small compared to the microscopic AFM interactions ($J' \approx 57$ K and $J \approx 39$ K at 2.1 GPa [30]), and because the couplings are frustrated the effective interaction scale may be even smaller. Experimentally, however, the M values are still very low as shown above, indicating that the effective AFM interactions still lock the spins strongly to the XY plane with very little canting

An important aspect of the magnetization is the absence of significant (not clearly detectable) discontinuity at the transition field; $H_c \approx 6.2$ T at 2.1 GPa in Fig. S5b. We do expect some discontinuity, similar to spin-flop transitions in uniaxially anisotropic quantum magnets, but, as we discuss further in Sec. S8, an anomalously small discontinuity observed here at the PS–AFM transition is likely a consequence of the emergent $O(3)$ symmetry associated with the nearby DQCP.

The small induced magnetization also makes it very unlikely that a magnetization plateau could exist up to the highest field strength reached here. Thus, our data do not support a supersolid phase at these fields and pressures. Different studies suggest that a much larger uniform magnetization is required to stabilize such a phase [28, 54].

S5. GAP ANALYSIS IN THE PS PHASE

The spin gap Δ of the lowest triplet excitations in the PS phase under applied field can be obtained by fitting the low-temperature spin-lattice relaxation rate $1/^{11}T_1$ to the form

$$1/T_1 \propto T^\alpha e^{-\Delta/k_B T}, \quad (\text{S10})$$

where α is a parameter to be determined. Theoretically, the T^α prefactor arises from the density of states and matrix element effects. In two dimensions, for a quadratic

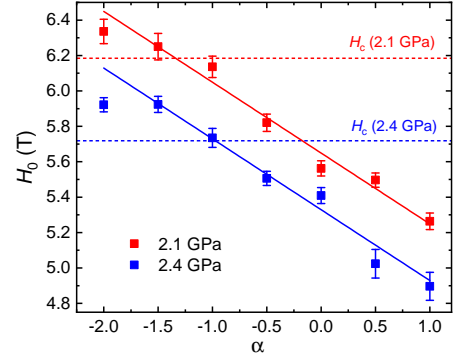


Figure S7. Gap closing fields H_0 from the fits in Fig. S6 graphed versus α at both pressures, 2.1 GPa and 2.4 GPa. The red (blue) dashed horizontal line is the value of H_c obtained at 2.1 GPa (2.4 GPa) from the analysis of the phase boundaries as discussed in Sec. S6 (results shown in Fig. 5f in the main text). The solid lines are linear fits, with the $\alpha = -2$ points left out because the value at 2.4 GPa deviates significantly from such a form.

dispersion of triplet excitations above the gap, $\alpha = 1$ if the matrix elements are constant. However, the matrix elements typically exhibit divergent singularities at the gap edge, which can lead to negative values of α .

Here we regard α in Eq. (S10) as an empirical parameter to be determined from the experimental data. Given the rather small amount of data, optimizing α just based on the goodness of the fit is not possible, as a wide range of values result in statistically acceptable fits. Figs. S6a and S6b show results for the field dependent gaps obtained from fits of $1/T_1$ at 2.1 GPa and 2.4 GPa, respectively, to a series of values of α .

To determine the best value of α in Eq. (S10), we next fit the gap values by a linear function $\Delta \propto (H_0 - H)$, with the zero-gap field H_0 and the overall factor as fitting parameters. We use the data points for which the gap is not very small (roughly for $\Delta/K_B \gtrsim 0.5$ K), and fitting is then possible only for $\alpha \leq 1$. Here we do not take a discontinuity at H_c into account, but for consistency with H_c we know that H_0 resulting from our procedure must be above the critical field; $H_0 > H_c$. Knowing H_c from our other measurements, we can then also extract a bound for α .

The H_0 values obtained by gap fitting for different α (using the range of points roughly consistent with linearity in each case) are plotted against α in Fig. S7. Here we can see that $H_0 > H_c$ only for $\alpha \leq -1$, thus establishing the upper bound on α (further supported by the linearity being poor in the small-gap regime for α larger than this value). Moreover, for $\alpha = -2$, the form of the gap versus H in Fig. S6 appears to deviate more from a straight line than it does for $\alpha = -1.5$. We also note that $\alpha = -2$ in Eq. (S10) would imply an unusually strong divergence of the spectral function at the gap edge, thus making such a large negative α value unlikely also from a fundamental perspective. Overall, this analysis suggests that α should

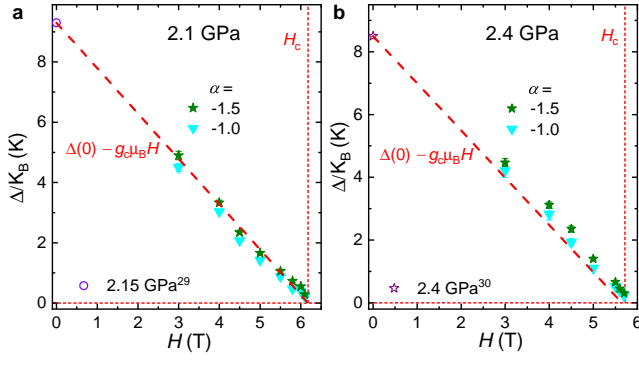


Figure S8. Gaps obtained by fits of $1/T_1$ to the form Eq. (S10) with $\alpha = -1$ (triangles) and $\alpha = -1.5$ (stars) at 2.1 GPa in **a** and 2.4 GPa in **b**. The dashed lines are the predictions based on the previously extracted $H = 0$ gaps from inelastic neutron scattering measurements at 2.15 GPa [29] (only slightly above 2.1 GPa in our experiments) in **a** and from the specific heat measurements at 2.4 GPa [30], in **b**. The vertical dashed lines mark the critical field at each pressure, determined by phase boundary analysis in Sec. S6.

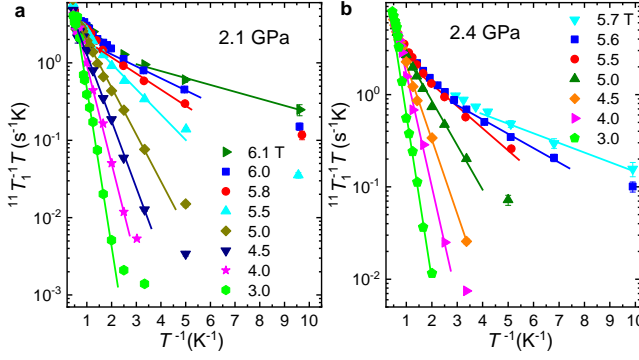


Figure S9. $T/^{11}T_1$ data sets for different field strengths corresponding to the PS phase at low temperatures, shown on logarithmic axes as functions of $1/T$ at pressure 2.1 GPa in **a** and 2.4 GPa in **b**. The solid straight lines are fits to the gap function $T/T_1 \propto e^{-\Delta/k_B T}$ with spin gap Δ .

be in the range -1 to -1.5 .

In practice, the gaps versus H for $\alpha = -1$ and -1.5 look very similar, and we cannot determine which of these values is better. In Fig. S8 we show our results for the two α values along with the linear $H > 0$ gap predictions based solely on the previously measured $H = 0$ gaps [29, 30], $\Delta(H) = \Delta(0) - g_c \mu_B H$, applicable for an $S = 1$ excitation, with the previously determined $g_c = 2.28$ [53]. Though there is of course some scatter among our data points, the overall agreement is remarkably good. We judge that overall $\alpha = -1$ is slightly better than -1.5 and show results for the former in Fig. 6a in the main text. A likely very small discontinuous jump of the gap at H_c is barely distinguishable from zero within the error bars both in Figs. S8a and S8b. In Sec. S8C we discuss the small gap discontinuity further in the context of modeling the PS–AFM transition with the CBJQM.

We finally show the $1/^{11}T_1$ data along with the $\alpha = -1$ fits in Figs. S9a and S9b, where $T/^{11}T_1$ at each field is plotted as a function of $1/T$ on semi-log axes. At the low-temperature (high $1/T$) side, the data fall on a straight line for each field, which indicates a gapped behavior with the assumed power-law correction with $\alpha = -1$. At very low values of $1/T_1$ in Fig. S9 deviate significantly from the fitted lines, likely because of weak disorder effects. We have not included those points in the fits.

S6. ANALYSIS OF EXPERIMENTAL PHASE BOUNDARIES

In the main text, we have fitted to two different functional forms of the PS and AFM transition temperatures, both of which are shown in Fig. 5f. We here further motivate these forms and explain the details of our fitting procedures; first for the modified critical forms in Sec. S6 A and then in Sec. S6 B for the logarithmic form expected for the PS ordering temperature at a first-order transition with emergent continuous order-parameter symmetry.

We stress that both fitting forms should have their ranges of validity in terms of the distance to a DQCP. Under the conditions of our experiments, these ranges of validity may both be marginal and partially overlapping. Thus, while we cannot determine which type of fit is the best, they both lend support to a simultaneous transition of both order parameters at a point (H_c, T_c) with very low T_c (in relation to the microscopic energy scales J and J' of the interacting spins and also to the transition temperatures away from H_c) and the direct-transition field H_c close to 6 T (weakly decreasing with increasing pressure). Below T_c , the direct field-driven PS–AFM transition is first-order for the range of pressures we have reached, less strongly at 2.4 GPa than at 2.1 GPa.

A. Critical point with emergent symmetry

It is tempting on the basis of Fig. 5f of the main text to fit our data for $T_{P,N}$ directly to the form expected at a QCP, i.e., $T_{P,N} \propto |H - H_c|^{\nu z}$. At a DQCP, the dynamical exponent is $z = 1$ and, for the most well studied case of the transition from an $O(3)$ AFM to a four-fold degenerate dimerized state, the emergent symmetry is $SO(5)$ and the correlation-length exponent ν has been estimated by QMC simulations to $\nu \simeq 0.46$ [12, 14, 55] (which applies to both the PS and the AFM order parameter). At a PS–AFM DQCP in zero field the emergent symmetry should instead be $O(4)$ on account of the PS order parameter being a scalar instead of the two-component dimer order parameter. In this case a similar value of ν as above was obtained [45].

In the presence of an external magnetic field the symmetry is further reduced to $O(3)$ at a putative DQCP separating phases with scalar PS and $O(2)$ AFM order

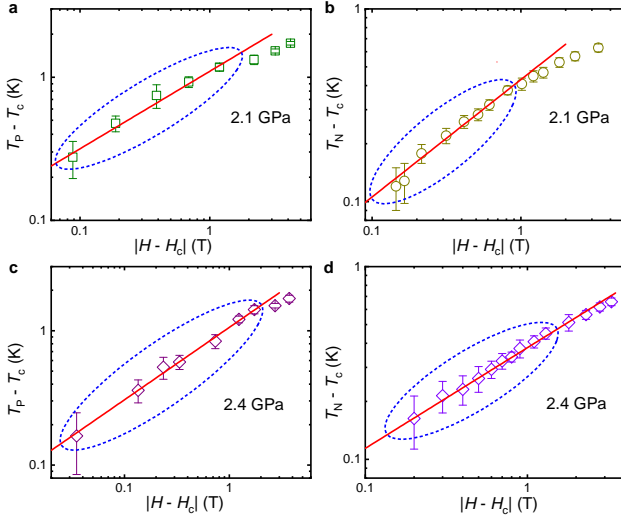


Figure S10. **Fits of the transition temperatures.** Power-law scaling of $T_{P,N} - T_c$ with $|H - H_c|$ obtained by four-parameter fits to each set of data using the near-critical form of Eq. (S11), shown for the experimental pressures 2.1 GPa (**a, b**) and 2.4 GPa (**c, d**). Each fit (straight line) applies to the data (open symbols) enclosed within the dashed ellipses, in a range about 1 T away from the critical fields.

parameters. For this DQCP, ν has not been determined, but, in analogy with the slowly evolving exponents of the conventional $O(N)$ transitions (where there is only one order parameter), one can expect that ν would remain close to its $SO(5)$ and $O(4)$ values. It is also very possible that the $O(3)$ DQCP does not strictly exist but is a weakly first-order triple point, at which scaling properties may still be governed by the $O(4)$ DQCP as long as the external field is not very large, i.e., the zero-field system is close to the DQCP. This closeness to $O(4)$ symmetry is supported by the very small field-induced magnetization at H_c in Fig. S5, i.e., the AFM order parameter is still $O(3)$ here for all practical purposes and can combine with the scalar PS order to form an effectively $O(4)$ emergent symmetry.

An argument against the above identical treatment of the PS and AFM transition temperatures is that $T_N = 0$ in an ideal 2D system, i.e., the system orders only exactly at $T = 0$ on account of the continuous order parameter symmetry (which precludes $T > 0$ ordering by the Mermin-Wagner theorem). In our case of $O(3)$ AFM symmetry reduced to $O(2)$ by a magnetic field there is a Kosterlitz-Thouless (KT) transition into a critical phase existing down to $T = 0^+$, which we do not consider further.

In $\text{SrCu}_2(\text{BO}_3)_2$, the weak 3D couplings allow for order also at $T > 0$, as we have found experimentally with T_N overall about half of T_P at comparable distances from H_c (Fig. 2d in the main paper). The 3D couplings also imply $T_c > 0$, and, therefore, the standard critical forms of T_P and T_N have to be modified. Phenomenologically,

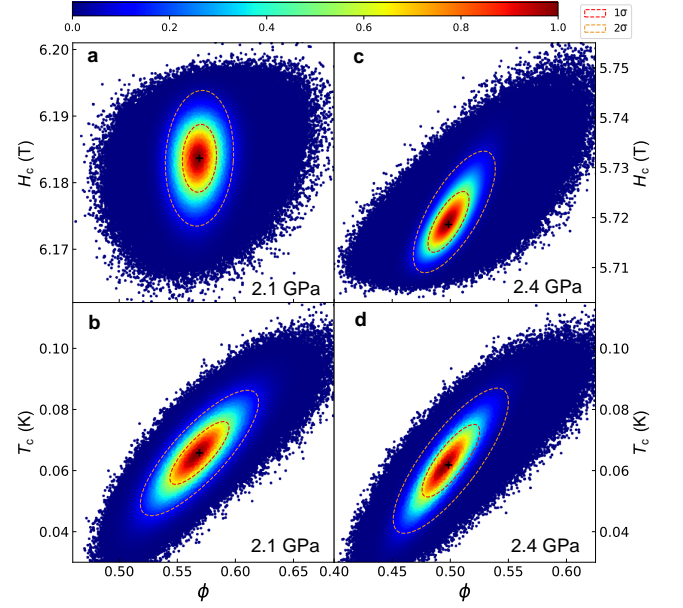


Figure S11. Contour maps of the fitting probability function projected on the space of the parameter pairs (H_c, ϕ) (**a, c**) and (T_c, ϕ) (**b, d**) at 2.1 GPa (**a, b**) and 2.4 GPa (**c, d**). Crosses mark the best fits and dashed lines the 1σ (68% CI) and 2σ (95% CI) intervals. These probability functions are based on the analysis of $N = 12$ data points at each pressure.

the form

$$T_{P,N} = T_c + a|H - H_c|^\phi, \quad (\text{S11})$$

where we have defined $\phi = z\nu$, can be used.

We first fit T_P and T_N independently, each with four parameters T_c , H_c , a and ϕ , following the Bayesian inference procedure [49] briefly described in the Methods section, with data errors included. Data in about 1 T range from the critical fields are used to obtain reasonable power-law fitting. The quality of the fits are depicted in Fig. S10, with H_c and T_c as below. With statistics within the 95% credible interval (equivalent to 2σ), at 2.1 GPa, the fit to T_P gives $H_c = 6.189 \pm 0.017$ T, $T_c = 0.074 \pm 0.026$ K, $\phi = 0.542 \pm 0.053$, and the fit to T_N gives $H_c = 6.185 \pm 0.017$ T, $T_c = 0.070 \pm 0.025$ K, $\phi = 0.609 \pm 0.107$; at 2.4 GPa, the fit to T_P gives $H_c = 5.731 \pm 0.016$ T, $T_c = 0.065 \pm 0.025$ K, $\phi = 0.533 \pm 0.060$, and the fit to T_N gives $H_c = 5.700 \pm 0.017$ T, $T_c = 0.067 \pm 0.024$ K, $\phi = 0.522 \pm 0.103$.

As shown above, the values of H_c , T_c , and ϕ obtained from T_P and T_N at each pressure are consistent within the errors. Therefore, it is reasonable to assume the same value of ν for both order parameters, which again is motivated in light of the expected duality of the PS and AFM phases [13, 45]. Considering that the two transitions meet at a bi-critical point (H_c, T_c) , a general fitting form

$$T_{P,N} = T_c + a_{P,N}|H - H_c|^\phi \quad (\text{S12})$$

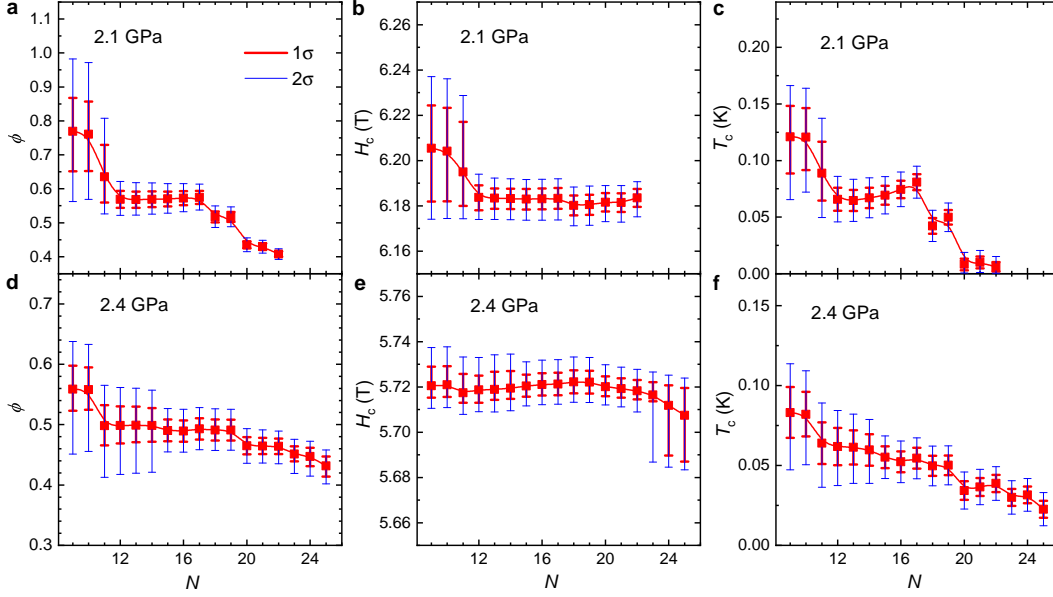


Figure S12. Critical parameters ϕ , H_c , and T_c obtained by fitting the data at 2.1 GPa and 2.4 GPa to the form of Eq. (S12), shown as functions of the total number, N , of data points used in the fitting procedure. Red and blue error bars mark respectively the 1σ and 2σ uncertainties of the fitting parameters obtained with each N . The solid lines are guides to the eye.

can be applied. A poor fit to the above form would indicate a more generic first-order transition.

To use Eq. (S12), it is important to establish the width of the critical regime, i.e., where H is sufficiently close to H_c for the scaling form to apply, while, in the present case where $T_c > 0$, the transition temperatures also exceed T_c . To obtain the five fitting parameters in Eq. (S12) describing the field-dependent transition temperatures measured at each of the two pressure values, the Bayesian inference procedure [49] is again applied.

The output of the process of sampling the parameters is a multidimensional probability distribution, and we first visualize this in Figs. S11a-S11d by showing projections of the distribution that illustrate its dependence on ϕ , H_c , and T_c , for the two measurement pressures. It is clear that the distributions specify a single well defined maximum in the space of each parameter, with narrow intervals of uncertainty in the parameters that reflect the error bars inherent to the data.

Before discussing the optimal parameter values determined by the fitting procedure, it is necessary to establish the unknown width of the critical scaling regime. For this we performed the analysis using $9 \leq N \leq 25$ data points, ordered in magnetic field by their separation from H_c , and in Fig. S12 we show the evolution of the optimal fitting parameters ϕ , H_c and T_c with N . One may anticipate a deteriorating fit at large N , where the points no longer obey critical scaling, and at small N , where there are simply too few points to extract a reliable functional dependence. Indeed we observe that as N is decreased below 20, all the fitting parameters for both pressures converge towards values that are nearly constant over the range $12 \leq N \leq 16$. However, for $N < 11$ the fit-

ting becomes less reliable and we neglect these estimates. Thus we take the parameters to follow for $N = 12$, where the data at both pressures show good convergence to a reliable fit.

Another means of demonstrating the quality of the near-critical fit and the width in field of the critical scaling regime is to show the dependence of $|T_{P,N} - T_c|$ on $|H - H_c|$ on logarithmic axis, as we do in Figs. S13a and S13b. In this form, data in the critical regime fall on straight lines whose gradient is ϕ , and scaling of T_P to T_N is ensured by the ratio of the prefactors, a_N and a_P , obtained from the Bayesian procedure. Only very close to H_c do some points deviate from the expected fit, which nevertheless lies well within their error bars (expanded by the logarithmic axes), because of the difficulty we have in identifying $T_{P,N}$ in this regime. Far from H_c , we find that many more than $N = 12$ data points are well described by the critical scaling form with a single exponent ϕ , and the fact that T_P and the T_N continue to fall on the same crossover curve out of the scaling regime underlines the duality between the PS and AFM ordered phases. From Figs. S13a and S13b we conclude not only that the critical fit is fully consistent but also that the width of the critical regime extends well beyond 1 T in both directions ($N = 17$ at 2.1 GPa and $N = 20$ at 2.4 GPa).

Returning now to the projected probability distributions as functions shown in Figs. S11a-S11d, the optimized fitting parameters, with uncertainties determined from the the 2σ level, are $H_c = 6.184 \pm 0.010$ T, $T_c = 0.066 \pm 0.020$ K, $\phi = 0.569 \pm 0.040$, and $a_N/a_P = 0.378 \pm 0.034$ for $P = 2.1$ GPa and $H_c = 5.719 \pm 0.012$ T, $T_c = 0.062 \pm 0.023$ K, $\phi = 0.498 \pm 0.070$ and $a_N/a_P = 0.367 \pm 0.030$ for $P = 2.4$ GPa. The errors presented in

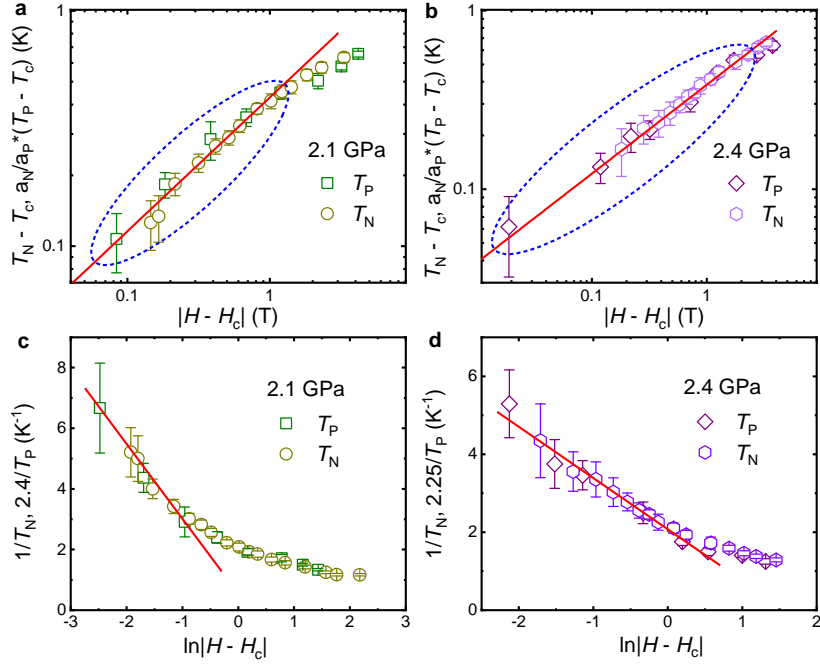


Figure S13. **Fits of the transition temperatures.** **a,b** Power-law scaling of $T_{P,N} - T_c$ with $|H - H_c|$ obtained by five-parameter fits to the data using the near-critical form of Eq. (S12), shown for the experimental pressures 2.1 GPa in **a** and 2.4 GPa in **b**. A constant factor a_N/a_P is used to scale T_P and T_N to the same y axis. Although the fitting was performed by monitoring convergence to the form given by the first 12 data points (straight red lines), this form applies to all of the data enclosed within the dashed ellipses, thus specifying the width of the critical scaling regime. **c,d** Inverse transition temperature shown as a function of $\ln|H - H_c|$, following the logarithmic form of Eq. (S14). The rescaling factors were taken from a_N/a_P in panels **a** and **b**, where the pressures are the same as in **c** and **d**, respectively.

the main text are at the 1σ level (68% credible interval). The most important single property of these fits is the remarkably low value of T_c at both pressures. Critical values of order 0.06 K are more than one order of magnitude below the typical (non-critical) values of both T_P and T_N , which is not a feature of a generic bicritical or triple point and strongly suggests that the finite T_c is a weak, or residual, effect, for example one arising from 3D perturbations to a system controlled by 2D physics.

Turning to the critical exponent, ϕ , we observe at the 2σ level that our 2.1 GPa result, $\phi = 0.569 \pm 0.040$, and our 2.4 GPa result (which has a somewhat larger error bar), $\phi = 0.498 \pm 0.062$, are mutually compatible. Certainly the exponent at 2.4 GPa, a pressure we have argued appears close to the DQCP of $\text{SrCu}_2(\text{BO}_3)_2$, is compatible with the estimates obtained for the $\text{SO}(5)$ DQCP, $\phi = z\nu$ with generically $z = 1$ and $\nu \approx 0.46$ [12, 55]. A very similar value has been obtained for the $\text{O}(4)$ case [45], which is the more likely type of DQCP controlling the behavior here.

In the $\text{O}(4)$ DQCP case, the model system studied in Ref. [45] has anisotropic, planar spin interactions, i.e., $\text{O}(2)$ AFM order parameter, and four-fold degenerate dimerized state. However, it has been argued [38] that the DQCP is the same as that obtaining when a scalar PS order parameter combines with an $\text{O}(3)$ AFM order parameter. It is not clear whether an $\text{O}(3)$ DQCP exists (to

our knowledge this case has not yet been considered theoretically), but given the extremely small uniform magnetization at the PS-AFM transition in $\text{SrCu}_2(\text{BO}_3)_2$ (Sec. S4), it is possible that the relevant DQCP in this case is still the $\text{O}(4)$ one. In other words, the uniaxial deformation of the $\text{O}(4)$ symmetry is insignificant at the temperatures $T \gg T_c$ for which we study critical scaling.

B. Logarithmic analysis

Given that at least the 2.1 GPa system has a rather strongly discontinuous behavior of the AFM order parameter (Fig. 4c of the main text), the applicability of the near-critical form Eq. (S12) of the transition temperatures can be questioned. The very low T_c values compared to the transition temperatures when H is not close to H_c is then unusual and calls for a mechanism not requiring very close proximity to a QCP. As we have discussed in the main text, emergent symmetry induced by a 2D DQCP far into a first-order line is such a mechanism.

In an ideal 2D system with an $\text{O}(N)$ order parameter and $N > 2$, a perturbation making one component of the interactions larger pushes the system to the “Ising side,” where it has an excitation gap and undergoes a finite-temperature phase transition with a scalar order param-

eter. In contrast, a perturbation making one component smaller still has a continuous order parameter symmetry, $O(N-1)$, and there can be long-range order only at $T=0$ (with a quasi-ordered KT phase at $T>0$ in the special case $N=3$).

A renormalization-group analysis of the Heisenberg model ($N=3$) with this type of anisotropy [44] deduced a logarithmic form of the transition temperature on the Ising side; the same analysis should also apply to $N>3$. In the CBJQM at zero external field, a first-order PS–AFM transition was found with a coexistence state whose order-parameter distribution indicated the emergence of $O(4)$ symmetry up to the largest system sizes studied, $L \simeq 100$ [7]. Then, moving into the PS side corresponds to a uniaxial deformation of the order parameter and the logarithmic form is expected; specifically [44]

$$T_P(g < g_c) = A \ln^{-1} |C(g_c - g)|, \quad (\text{S13})$$

where $g = J/Q$. This form was also confirmed in Ref. [7] for g close to g_c . In the most likely scenario, the emergent symmetry is violated at some long length scale Λ , corresponding to some small energy scale ϵ (which can be taken as the gap of the Goldstone mode that corresponds to the Ising direction). The above form should then only be valid down to T_P of order ϵ , but this energy scale was not reached in Ref. [7].

In our experiments on $\text{SrCu}_2(\text{BO}_3)_2$, we study the phase transitions at fixed pressure versus the magnetic field, and the emergent symmetry is reduced to $O(3)$. Also in this case must there be a smooth approach of T_P to 0 (assuming now momentarily that the symmetry is asymptotically exact) and Eq. (S13) should apply with $g_c - g$ replaced by $(H_c - H)^a$, where the exponent a accounts for the different forms of gap closing versus g and h ; $(g_c - g)^{1/2}$ [44] and $H_c - H$, respectively. However, the value of the exponent can be absorbed into the factor of proportionality and we do not need to consider it further.

Experimentally, we expect violations of the $O(3)$ symmetry not only from the fundamental 2D effect related to the distance to the DQCP, but also because of 3D effects (and potentially other sources, like impurities, that we have not discussed). Thus, the logarithmic form should break down below some temperature. As in the case of the near-critical form Eq. (S12), we may again add T_c as an offset optimized in the fitting procedure. However, our fits to are actually optimal with $T_c = 0$, i.e., Eq. (S13) without any added constant, though statistically acceptable fits are also obtained with T_c values up to those obtained in the previous section. The fit shown in Fig. 5f of the main paper are for zero offset, and the further analysis presented below also was done with $T_c = 0$.

It is not immediately clear whether the AFM transition temperature can also be incorporated into a common fitting form in this case. Interestingly, however, weak inter-layer (3D) couplings J_\perp between 2D Heisenberg AFM layers also leads to a logarithmic form; $T_N(J_\perp) = \ln^{-1}(C/J_\perp)$ [44]. In the experiments the microscopic coupling J_\perp is fixed, but it is still possible that an effec-

tive, “renormalized” 3D coupling $J_\perp(H)$ can be defined, in light of the fact that 2D AFM order is present only above H_c and increases with H . Thus, we assume here that both transition temperatures take the common form

$$T_{P,N} = A_{P,N} \ln^{-1} |C_{P,N}(H - H_c)|, \quad (\text{S14})$$

though we are less confident in the form of T_N than T_P and only show results for the latter in Fig. 5f of the main paper. Here we will discuss both transitions.

At both pressures, 2.1 and 2.4 GPa, the optimal H_c value is statistically indistinguishable from the value obtained using the near-critical form of Eq. (S12). To gauge the quality of the logarithmic fit, in Figs. S13c and S13d we show the inverse transition temperatures on semi-log axes. The logarithmic fit remains valid over a significantly larger range of fields at 2.4 GPa (where it includes 15 data points) than at 2.1 GPa, which would indeed be expected if 2.4 GPa lies closer to the DQCP, because the emergent symmetry would then be better established (i.e., manifested on longer length scales).

Although the near-critical forms in Figs. S13a,b remain valid somewhat further away from H_c , corrections are expected here in both cases, and the non-universal width of the scaling regime is not a criterion for selecting the best critical form. As mentioned in the main text, each of the fitted forms has its range of validity in principle, but the experiments may be in a cross-over region where there are corrections to both forms but they still work reasonably well.

S7. QUANTUM-CRITICAL SCALING OF $1/T_1$

A quantum-critical point at $T_c = 0$, reached at some tuning parameter $g = g_c$, should be associated with a $T > 0$ scaling regime [56], often referred to as the “critical fan” because of its shape extending out from the $T = 0$ point into a wide region in the (g, T) plane. Scaling in the critical fan is one of the most distinctive and important consequences of quantum criticality, reflecting detectable far-reaching influence of the $T = 0$ critical point even when this point itself cannot be reached.

The most extensively studied example of $T > 0$ quantum criticality is in a class of 2D quantum antiferromagnets with two exchange constants J_1 and J_2 (reviewed in Ref. [57]), where the J_2 -coupled spins form dimers (and all spins belong to a dimer). As a function of the ratio $g = J_2/J_1$, the ground state is a Néel AFM for $g < g_c$ and a unique dimer singlet state for $g > g_c$. Unlike the PS state of the SSM, there is no spontaneous symmetry breaking in this gapped phase. There is no $T > 0$ order in the system for any g , but different low-temperature regimes with distinct physical properties can be defined by two macroscopic energy scales; the spin stiffness ρ_s for $g < g_c$ and the gap Δ for $g > g_c$. Both these energy scales vanish continuously as $g \rightarrow g_c$, and the critical fan is roughly located at temperatures above ρ_s for $g < g_c$

and above Δ for $g > g_c$. In other words, in the critical fan T is the dominant energy scale.

At g_c , the quantum-critical scaling regime extends all the way down to $T = 0$, while for $g \neq g_c$ the curves $\rho_s(g)$ and $\Delta(g)$ define smooth cross-over boundaries to different low-temperature behaviors, called renormalized classical and quantum disordered, respectively [46]. Upon increasing T , the critical behavior controlled by the point $(g_c, T_c = 0)$ must break down when (or before) the correlation length decreases to order one lattice spacing, where the continuum description of the system (upon which critical behaviors rely) is no longer valid.

In systems with $T > 0$ phase transitions, on one or both sides of g_c , the transition temperature(s) vanish as $g \rightarrow g_c$ and a critical fan should still exist, either bordered by two ordered $T > 0$ phases or by a single ordered phase and an energy scale in a disordered phase as discussed above. In the case of $\text{SrCu}_2(\text{BO}_3)_2$, we expect a critical fan in the (H, T) plane (i.e., in the notation above, $g = H$) between the PS and AFM phases. The fan does not necessarily extend down all the way to the phase boundaries if these boundaries are themselves thermal phase transitions, which are governed by their own critical behaviors. This is true for the AFM phase of $\text{SrCu}_2(\text{BO}_3)_2$, where gapless classical spin fluctuations may mask the 2D quantum critical fluctuations at the same staggered wave-vector. However, the PS ordering involves singlets, and its critical Ising-type plaquette fluctuations should be better decoupled from the quantum-critical spin fluctuations residing in a different part of the spin and momentum space. Thus, we expect the quantum-critical spin fluctuations to reach close to the PS phase boundary in phase diagrams such as Fig. 5f.

Scaling behaviors in the critical fan of the O(3) transition in the aforementioned Heisenberg spin systems have been derived using field-theory approaches for a number of physical observables [46] and detailed comparisons have been carried out with results of numerical simulation studies of spin Hamiltonians (with Ref. [58] being perhaps the most detailed study).

In the case of the spin-lattice relaxation rate, the expected general behavior in the fan extending from any quantum-critical point of a 2D system should be $1/T_1 \propto T^{\eta/z}$, where η is the standard critical exponent governing the power-law decaying spin correlations and z is the dynamic exponent (see the SI of Ref. [59] for an elementary derivation). Assuming $z = 1$, which is the case for a DQCP, we have $1/T_1 \propto T^\eta$, ideally for arbitrarily low temperatures exactly at $g = g_c$. Slightly away from g_c , the same power law applies, but with a constant correction $b(g)$ [46];

$$\frac{1}{T_1} = b(g) + aT^\eta, \quad (\text{S15})$$

where $b(g_c) = 0$ and the sign of $b(g)$ is negative or positive in the gapped and gapless phase, respectively. The factor a and the functional form of the additive contribution $b(g)$ are known (to some approximation) from analytical

calculations in some cases [46], but we are not aware of predictions for $1/T_1$ and a DQCP specifically.

In our experimental results for $\text{SrCu}_2(\text{BO}_3)_2$, we observe power-law scaling in what appears to be a quantum-critical region above the PS phase at 2.4 GPa (Fig. 5c). The exponent $\eta \simeq 0.20$ is much larger than the well known values $\eta \approx 0.03$ for the O(2) and O(3) critical points in 2+1 dimensions. The value is closer to results obtained with models realizing DQCP physics without magnetic fields [2, 12, 55], though we are not aware of results in the presence of a magnetic field. It should be pointed out here that the existence of DQCPs with various emergent symmetries is an ongoing area of research [13–15]. In the case at hand here, an O(3) symmetry would be naively expected but, as we discussed in, the very small observed magnetization at the AFM–PS transition point (S6 A) suggests that the DQCP controlling the critical behavior should be one with emergent O(4) symmetry. The cross-over from O(4) to O(3) symmetry upon moving away from the DQCP is further discussed in Sec. S8B. We here discuss further our evidence for near-criticality in $\text{SrCu}_2(\text{BO}_3)_2$ at the highest pressure studied, reflected in $T > 0$ scaling behavior of the form Eq. (S15) and presented in the main paper as Fig. 5e.

At first sight, a complication of the critical-fan scenario is that the common transition point T_c is not strictly zero. However, as indicated in Fig. 2b, we still expect a quantum critical fan above T_c if this temperature is much lower than the relevant energy scales of the adjacent phases. In the present case, those energy scales can be taken as the transition temperatures T_P and T_N , which increase rapidly for H away from H_c . In the case of the PS phase, above which our analysis here will be focused, T_P safely exceeds the extrapolated T_c value for H at and below 5.7 T at $P = 2.4$ GPa.

On the AFM side of the transition, at 5.8 T and higher field in Fig. 5d, we only have limited data above the peak that signifies the transition to long-range Néel order. This transition would be absent in a single 2D layer, which can undergo O(3) symmetry breaking only at $T = 0$. Already very weak 3D couplings J_\perp can push the transition temperature T_N to rather high values, since the dependence on J_\perp is logarithmic; $T_N \propto J_{2D}/\ln(J_{2D}/J_\perp)$ [44, 60], where J_{2D} is the effective magnetic coupling within the layers [61].

As seen in Fig. 5d, the ordering peak is quite broad, and none of the data above the peak show a reduction in $1/T_1$ with decreasing T . Thus, we are not able to analyze any predominantly 2D quantum-critical fluctuations here (and at higher temperatures, where we do not have data, the scaling behavior would be terminated when the classical paramagnetic regime above the critical fan is entered, as seen on the PS side). On the AFM side at 2.1 GPa, in Fig. 5b, we do have data at higher temperatures and the influence of the AFM ordering peak far above T_N is very clear. The quantum-critical spin fluctuations are visible in $1/T_1$ on the PS side, in Fig. 5c, because there is no spin ordering and the 3D magnetic couplings do not

play a significant role there.

In Fig. 5e we demonstrate consistency with the expected critical scaling form (S15) with a temperature independent shift. Since the field values correspond to the gapped phase, we expect $b_H \equiv b(H)$ (where we now replace the generic parameter g by the field strength) to be positive, approaching zero as $H \rightarrow H_c$. From general scaling arguments [46] we expect the form $b_H \propto (H_c - H)_0^d$ for H close to H_c , but we do not know the value of the exponent d . We therefore carry out a fitting procedure for the fields close to H_c , between 5.4 T and 5.7 T, where the exponent and the factor of proportionality are optimized for the best data collapse to the form Eq. (S15) of $1/T_1$, using the optimal value of the exponent on T ; $\eta = 0.20$. For the smaller field strengths we optimize the values b_H individually. The results for the so obtained $1/T_1(H) + b_H$ are shown in Fig. 5e, where the optimized b_H values along with the fitted power-law form are shown in the inset. The description of the experimental data with common power-law over almost a decade of temperature is apparent, along with the faster decays and more rapid increase (in the one case, $H = 5.4$ T, where we have data) at the lower and upper bound, respectively, of the critical scaling regime for given H .

Including our estimated error bars from the fitting procedure, our results are $\eta = 0.20 \pm 0.02$ and $d = 0.77 \pm 0.04$. The exponent η estimated for an O(4) DQCP from static correlation functions in a planar version of the J - Q model is $\eta_{JQ} = 0.13 \pm 0.03$ [45], thus marginally in agreement with our experiments.

An important aspect of the quantum critical scaling in $\text{SrCu}_2(\text{BO}_3)_2$ is its manifestation in our experiments only at 2.4 GPa, not at 2.1 GPa. At the lower pressure a substantial peak is instead seen in Fig. 5a, and this peak was interpreted as the PS ordering temperature according to the NMR line-width analysis in Fig. 3b and also considering the good agreement with the peak observed in the previous specific heat measurements [30, 31]. In our scenario outlined in Fig. 2, the system moves closer to the DQCP with increasing pressure, thus causing an increase in the spin fluctuations in the (T, H) regime between $T_P(H)$ and $T_N(H)$. It is at least plausible that these spin fluctuations also affect the strength of the PS ordering, i.e., the overall factor in the singlet density modulations below T_P [i.e., the factor a in the critical PS order parameter $m_p = a(T_P - T)^\beta$] is reduced when singlets “break”. Thus, even if the PS transition may have a broad precursor at higher T also at 2.4 GPa, this may not significantly affect $1/T_1$ until the spin excitations become gapped by the long-range PS order. The observed behavior without PS ordering peak in Fig. 5c supports this scenario. Note also that phase separation is only observed close to H_c on the AFM side of the transition (Figs. 4a,b).

Indeed, at the point (H_c, T_c) we know that the coexisting order parameters are weaker at 2.4 GPa—though only observed in the AFM order, Fig. 4c, a similar weakening of PS order should also be expected—and that trend

should persist also for the short-range PS order above T_P . That overall lowering of the plaquette strength should then also translate into less contributions to $1/T_1$ from the essentially classical plaquette fluctuations above T_P (which also impact $1/T_1$ less directly than the spin fluctuations), thus suppressing the peak at T_P . At 2.1 GPa, Fig. 5a, the depletion of spin fluctuations in the PS liquid phase until the formation of the ordering peak is obvious. While $1/T_1$ also decreases sharply for T above 2 K at 2.4 GPa (Fig. 5c), the abrupt change of behavior to the common power law points to another dominant source of spin fluctuations, which, as we have argued above, is the quantum criticality.

S8. FIELD-DRIVEN TRANSITIONS IN QUANTUM SPIN MODELS

To study the nature of the PS–AFM transition theoretically, we perform SSE QMC simulations of the CBJQM, as detailed in the Methods section. This model is related to the SSM [and, we argue, to $\text{SrCu}_2(\text{BO}_3)_2$] at least to the extent of hosting PS and AFM phases with the same order-parameter symmetries. While QMC simulations of the SSM in the J/J' regime of its QPTs are afflicted by a severe minus-sign problem [62, 63], the CBJQM is fully accessible to QMC simulations and, thus, offers unique opportunities for quantitative studies of the universal aspects of the PS–AFM transition.

The PS–AFM transition in the CBJQM has been shown at zero field to be of first-order in the sense that the PS and AFM order parameters coexist with finite values [7]. At a conventional first-order quantum phase transition, the coexistence state can be understood as an analogy to uniform thermodynamic states separated by free-energy barriers. The Hilbert space for a large system subdivides by energy barriers into separate parts for the two different ground states. On a finite lattice at $T = 0$, there is a characteristic time for tunneling between these parts of the Hilbert space that diverges with the system size. In a realistic situation in a material, spatial domains in different phases would form.

In the CBJQM [7] (and other related models [8, 10]) the coexistence state at the PS–AFM transition hosts emergent O(4) symmetry of the four-dimensional vector (m_x, m_y, m_z, m_p) , which combines the three components of the staggered (AFM) magnetization and the scalar PS order parameter. Here it should be noted that the Hamiltonian does not have any point in parameter space where such a symmetry is explicit, and the symmetry instead emerges on long length scales. The emergent continuous symmetry fundamentally changes the coexistence state. In a finite system the order can be continuously rotated between the AFM and PS states without passing through energy barriers. This type of coexistence of two ordered phases can also be characterized as a supersolid order, where two non-zero order parameters can coexist at the same spatial location. In the thermodynamic limit, the

$O(4)$ symmetry is broken (the time scale of rotations diverges), and any mix of AFM and PS order can be realized in principle. In practice, domain with different symmetry-breaking will form.

The most likely scenario is that the emergent symmetry is violated above some length scale, thus being reduced to $O(3) \times Z_2$ of independently fluctuating AFM and PS order parameters. In cases studied so far, which includes not only $O(4)$ symmetry [7, 8, 43] but also a model with four-fold degenerate PS state and emergent $SO(5)$ coexisting order parameter [10], this length scale can be at least hundreds of lattice spacings. The reduction of the $O(4)$ order parameter symmetry into $O(3) \times Z_2$ has been studied in detail when inter-layer couplings are turned on [43]. Here we characterize the putative $O(3)$ symmetry at the PS–AFM transition in the CBJQM when the $O(3)$ symmetry of the AFM order parameter is reduced to $O(2)$ by the external magnetic field. We will demonstrate clear analogies to behaviors observed experimentally in $\text{SrCu}_2(\text{BO}_3)_2$.

In addition to the CBJQM we also here study the anisotropic Heisenberg model, the $S = 1/2$ XXZ model defined in Eq. (S7), in which the symmetry of the order parameter changes versus λ . At zero magnetic field, for $\lambda < 0$ the ground-state is an XY AFM state with an $O(2)$ order parameter, while for $\lambda > 0$ the ground-state changes to an Ising phase with Z_2 order parameter. In this case, the transition between XY and Ising orders is clearly not first-order in the conventional sense; only the direction of the AFM order parameter in spin space flips discontinuously as the isotropic $O(3)$ point is crossed, while the magnitude of the order parameter does not change. The PS–AFM transition in the CBJQM at $h = 0$ is analogous to this “spin-flop” transition, though in this case the symmetry is not explicit but emergent. The two order parameters of the CBJQM would of course also not a priori be expected to form components of the same vector, and unless the transition is analyzed in detail it would appear to be a clear-cut case of a discontinuous jump between two completely different ordered states with unrelated symmetry breaking

When Ising-anisotropic, the XXZ model undergoes a spin-flop transition versus an external magnetic field, in this case from the Ising AFM phase to a canted XY AFM phase [64]. This transition is in some respects similar to the field-driven AFM state in the CBJQM, though there are important differences as we will elucidate below. One important aspect of these differences is that the discontinuities at the first-order transition are much more pronounced in the XXZ model when comparing systems with similar sized spin gaps at zero field. The small discontinuities that we find in the CBJQM lend support to our argument that it is a suitable model for describing the universal aspects of the PS–AFM transition that we have identified in $\text{SrCu}_2(\text{BO}_3)_2$.

We present results for the field-driven phase transitions of both models in Sec. S8 A. In Sec. S8 B we discuss the evidence for emergent symmetry in the CBJQM pro-

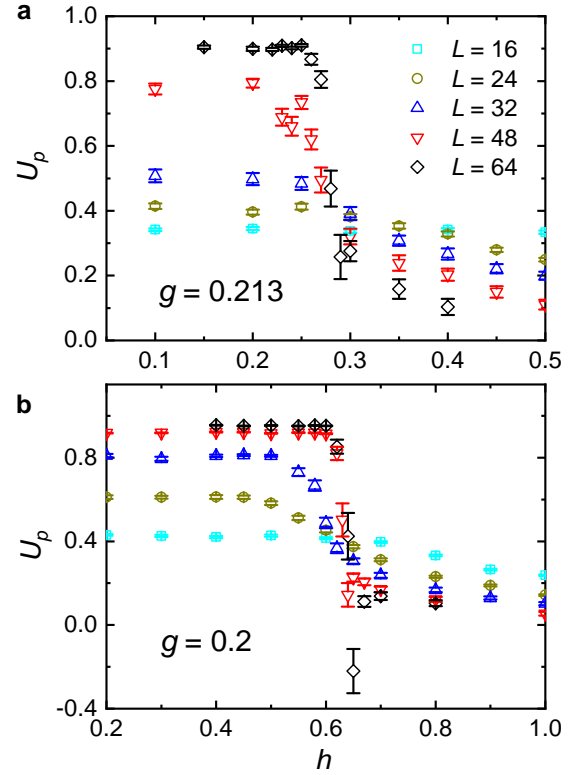


Figure S14. Binder cumulant of the PS order parameter of the CBJQM, shown as a function of the reduced field at $g = 1/4.7 \approx 0.213$ (in **a**) and $g = 1/5 = 0.2$ (in **b**). Simulations were performed for a range of system sizes up to $L = 64$ and at temperature $T = J/L$. The transition field, h_c , is determined from the crossing point of the $U_p(L)$ curves. The negative value of U_p close to h_c for the largest system size in panel **b** indicates an asymptotically conventional first-order transition.

vided by the histograms in Figs. 6d-f of the main text and further by the dimensionless cross-correlation ratio $\langle m_{xy}^2 m_p^2 \rangle / \langle m_{xy}^2 \rangle \langle m_p^2 \rangle$. In Sec. S8 C we discuss the spin gap, with examples of the field dependence for both the CBJQM and XXZ model. In Sec. S8 D we summarize our scenario for the PS–AFM transitions mechanism in the CBJQM.

A. First-order quantum phase transitions

As the first characterization of the field-driven phase transition of the CBJQM, we calculate the Binder cumulant of the PS order parameter,

$$U_p = \frac{3}{2} \left(1 - \frac{\langle m_p^4 \rangle}{3 \langle m_p^2 \rangle^2} \right), \quad (\text{S16})$$

where m_p is the order parameter of the PS phase, which we have defined in Eq. (S4). In the thermodynamic limit, the Binder cumulant obeys the properties $U_p \rightarrow 1$ in the PS phase and $U_p \rightarrow 0$ in the AFM phase. For a given

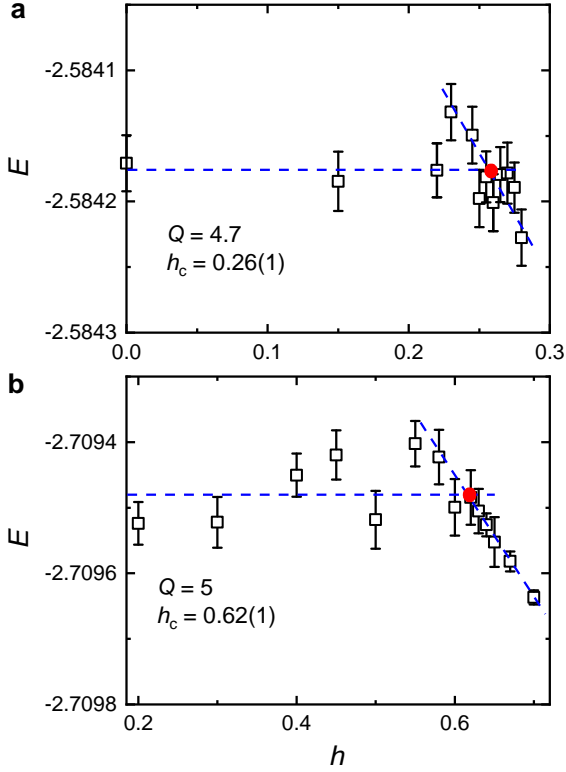


Figure S15. **a** Internal energy of the CBJQM at $Q = 4.7$ ($g \approx 0.213$) with system size $L = 48$ simulated at $T = 1/L$. The crossing of the two dashed lines fitted to the two branches give the transition field h_c marked with a red circle. **b** Same plot at $Q = 5$ ($g = 0.2$).

ratio $g = J/Q$ the transition field $h_c(g)$ can be extracted from the crossing point of the different curves, $U_p(L)$, obtained from calculations on systems of finite size, L .

Figure S14 shows such finite-size analysis for two model parameters, $g \approx 0.213$ ($Q = 4.7$, $J = 1$) in Fig. S14a and $g = 0.2$ ($Q = 5$) in Fig. S14b, both obtained in simulations at $T = J/L$ with maximum system size (length) $L = 64$. Here it should be noted that the PS ground state is a singlet, and a calculation exactly at $T = 0$ would deliver a constant value of U_p up to the point where a level crossing with the lowest magnetized state takes place. This h -independent constant value still depends on the system size, reflecting finite-size fluctuations of the order parameter. Almost constant values of U_p are indeed observed Fig S14a at small values of h , before a decrease that becomes sharper with increasing system size. The rounding before the transition at $h = h_c$ reflects finite-temperature effects, while for $h > h_c$ there are $T > 0$ effects as well as effects of the ground state magnetization evolving with h .

From the crossing point of the Binder cumulants for the two largest system sizes we obtain $h_c = 0.27 \pm 0.01$ for $g = 0.213$ and $h_c = 0.62 \pm 0.01$ for $g = 0.2$. We note that, at $g = 0.2$, U_p of the $L = 64$ system is not a monotonic function of h but drops to negative values near the

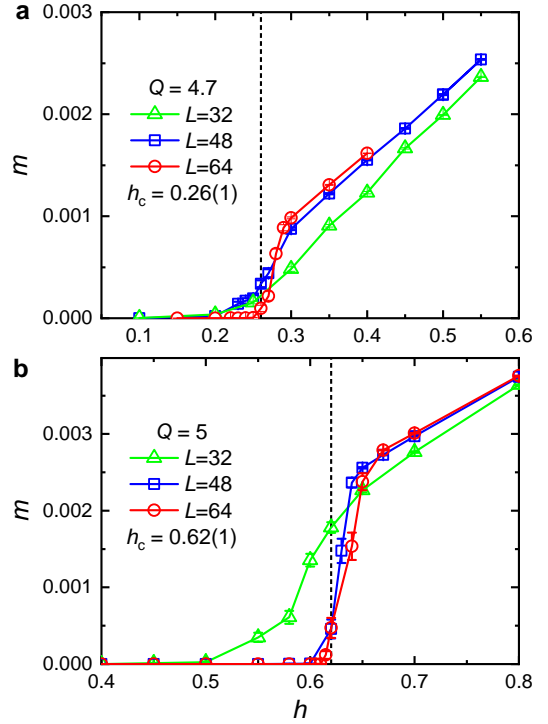


Figure S16. **a**: Magnetization per spin vs field strength in the CBJQM at $Q = 4.7$, simulated on lattices of size $L = 32, 48$, and 64 at temperature $T = 1/L$. **b**: The same at $Q = 5$.

transition in Fig. S14b. This behavior is characteristic of a conventional first-order transition [57]. At $g = 0.213$, the Binder cumulant remains positive up to $L = 64$ in Fig. S14a, though eventually, for larger system sizes, we also expect a negative peak to emerge at this coupling.

For the CBJQM at $h = 0$, no negative values of the Binder cumulants were observed up to system size $L = 96$ [7], which was taken as evidence (along with other signals) of an emergent continuous symmetry. If the higher symmetry is ultimately violated, we expect a conventional coexistence state and negative cumulant, as also seen in the CBJQM with weak inter-layer couplings [43]. Given that we observe a negative peak for the largest system in Fig. S14b, and also the overall sharp drop of the cumulant at h_c , we expect the putative $O(3)$ symmetry to also be violated on a scale of tens of lattice spacings, and this length scale should grow as $g_c(h)$ approaches its $h = 0$ value. We point out again that $g_c(h = 0)$ is not a critical point but a first-order transition with a very long length scale of emergent $O(4)$ symmetry, presumably induced by a DQCP slightly outside the parameter space of the CBJQM

The level crossing mechanism of the transition can be directly confirmed by studying the low-temperature internal energy versus the field. In Fig. S15 we show results for a system with $L = 48$ at two model parameters, $Q = 4.7$ ($g = 0.213$) in panel a and $Q = 5$ ($g = 0.2$) in panel b. In each case, two branches of the energy can be observed (with some effects of meta-stability). On

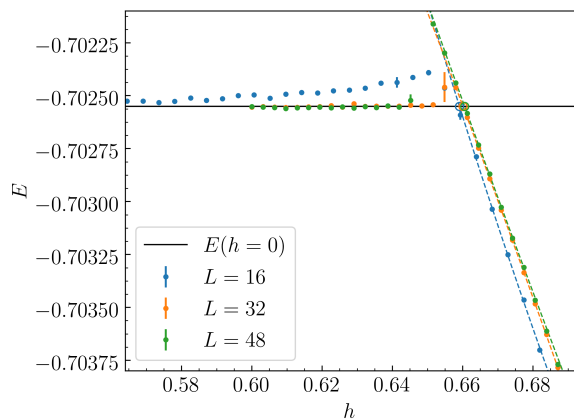


Figure S17. Energy per spin vs the field for the XXZ model at $\lambda = 0.1$ for systems of size $L = 16, 32,$ and 48 . The flat portion corresponds to the h -independent singlet ground state, which crosses a state with $m > 0$ at h_c . We extracted h_c from the crossing points of the fits shown. The horizontal lines show the $h = 0$ energy, which for $L = 16$ is slightly below the QMC values because of temperature effects at $\beta = L$ when the spin gap is small. No such effect is seen for $L = 48$. The higher branch for $h < h_c$ reflects metastability in the simulations close to the first-order transition.

the $h \leq h_c$ branch, the energy should be completely flat, while an almost linear behavior should be expected for $h > h_c$, reflecting the linear decrease of the energy of a level with non-zero magnetization and the increase of the magnetization with h . In Fig. S15, the error bars are large on the relevant small scale of the energy changes and we just fit a line also on this branch. The crossing point is fully compatible with h_c extracted above from the Binder cumulant. The small slope of the energy versus h for $h \gtrsim h_c$ reflects the weak nature of the first-order transition in this case.

Fig. S16 shows the field induced magnetization at both $Q = 4.7$ and 5 . A temperature rounded small jump (of about 0.25% of the saturation value) followed by a near-linear increase can be observed at $Q = 5$. At $Q = 4.7$, the jump is less than half as large and there are relatively larger effects of finite size and finite temperature. A priori, such small magnetization discontinuity is not expected for a system going through a first-order spin-flop transition. It should be stressed again that even at the $h = 0$ transition point at $Q \approx 4.6$ (Ref. [7] and Fig. 6b in the main text) the transition is distinctively first-order, in the sense of hosting substantial coexisting long-range PS and AFM order parameters.

As a bench-mark case further illustrating that the discontinuities observed here in the CBJQM versus the field are indeed small, we next present results for the field-driven transition out of the Ising phase of the XXZ model at $\lambda = 0.1$, where the transition field h_c is almost the same as that of the CBJQM at $Q = 5$. We again set the temperature $T = 1/L$ and have studied systems of size up to $L = 48$. Figure S17 shows the internal energy per spin versus h for three different system sizes. Here

we clearly observe meta-stability for the largest system, while the smallest system can still fluctuate enough to produce an energy slightly above the true ground state energy (which of course is h independent for $h < h_c$). Fitting lines to the two energy branches, we see that the transition point is well converged at $h_c = 0.660$. Though the transition field is comparable to those of the CBJQM at $Q = 5$ (which also implies comparable $h = 0$ gaps in these two systems), the meta-stability in the XXZ model is much more prominent than in Fig. S15.

The magnetization versus the field is shown for the same system sizes in Fig. S18. Here the jump in m is more than 20 times larger than that of the CBJQM at $Q = 5$ (Fig. S16a) even though the values of h_c and $\Delta(h = 0)$ are almost the same. Thus, judging from both the energy and the magnetization, the transition in the XXZ model is much more strongly first-order, even though the relevant energy scales (h_c or the $h = 0$ gap) of the two models are comparable (within 10% of each other), and at first sight the transition mechanism is the same.

An important difference between the conventional spin-flop transition in the XXZ model and the PS-AFM transition is that the magnetic field does not explicitly couple to the objects (plaquette singlets) forming the PS order parameter. In contrast, in the XXZ model the magnetic field couples to the uniform Fourier component of the spins, and the Ising order parameter is the staggered component of the same spins. The magnetic field in the CBJQM explicitly deforms only the AFM order, taking it from $O(3)$ to $O(2)$ symmetric while leaving the PS state essentially intact. Thus, with emergent $O(4)$ symmetry at the PS-AFM transition at $h = 0$, it is not surprising if an $O(3)$ symmetry survives after one of the components of the AFM order has been suppressed by $h > 0$. Because of the level crossing, the transition is still eventually first-order with no exact $O(3)$ symmetry, but the influence of the $O(4)$ DQCP (existing in an extended parameter space) is much more robust than the influence of the exact $O(3)$ point on the order parameters at the spin-flop transition in the XXZ model.

B. Emergent $O(3)$ symmetry

Our numerical test of an emergent $O(3)$ symmetry in the CBJQM, shown in Figs. 6d-6f of the main text, is based on the probability distribution function of the PS order parameter, m_p , across the QPT. An $O(3)$ symmetry would combine m_p with the two XY-AFM order parameters to form a three-component supervector, $\mathbf{n} = (m_x, m_y, m_p)$, which has a uniform probability distribution on the sphere of the order-parameter space

$$\mathbf{n}^2 = R^2, \quad (\text{S17})$$

where R is the radius of the sphere. Specifically, integrating out the m_x and m_y components gives the distribution

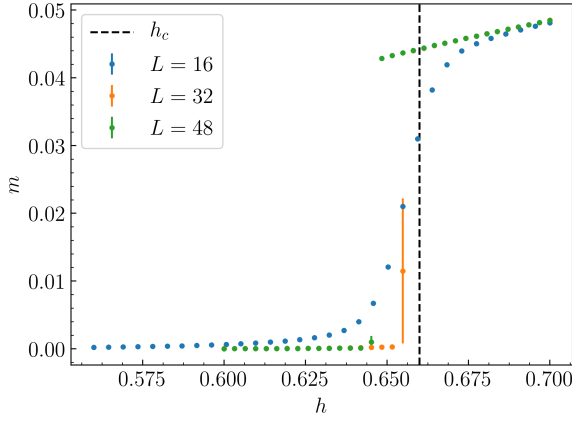


Figure S18. Magnetization per spin in the same XXZ simulations as in Fig. S17. For $L = 32$, one very large error bar reflects a simulation that escaped from the meta-stable state during the simulation. The transition point determined from the results in Fig. S17 is shown with the vertical dashed line.

of m_p in the presence of an $O(3)$ symmetry as

$$P(m_p) = \begin{cases} 1/(2R) & \text{for } |m_p| \leq R, \\ 0 & \text{for } |m_p| > R, \end{cases} \quad (\text{S18})$$

whence the expectation of a uniform distribution over a region of finite width centered at 0 when the system is very close to the transition point, h_c .

The probability distributions given by our simulations (Figs. 6d-6f of the main text) do indeed bear out this expectation: the double-peak structure of $P(m_p)$ in the PS phase reflects a Z_2 symmetry, which is broken in the thermodynamic limit (where the peaks become δ -functions). The AFM phase is marked by a single peak centered at $m_p = 0$, because its order and symmetry-breaking take place in a different channel (namely, breaking of global spin-rotation symmetry). Right at h_c , the clear plateau feature in $P(m_p)$ indicates that the emergent symmetry is $O(3)$. The rounding of the edges can naturally be explained by finite-size effects, which correspond to a fluctuating radius R of the sphere in Eq. (S18).

The results in Figs. 6d-6f were generated for a system size $L = 32$. It is difficult to obtain statistically good results (smooth histograms) for larger sizes, because of the long autocorrelation time (which grows rapidly with the system size) in the simulations. Given the negative cumulant peak in Fig. S14, we would expect to see a three-peak structure developing in place of the flat portion of the distribution in Fig. 6e for larger system sizes. However, the observation of the signatures of $O(3)$ symmetries for $L = 32$ already demonstrates that this symmetry is emergent. The symmetry is likely inherited from an $O(4)$ DQCP when the magnetic field is turned on, through an extension of the mechanism for first-order transitions with emergent $O(4)$ symmetry discussed in Ref. [8]. Here we also point out that the sum of the distributions in Figs. 6d (in the PS state) and Figs. 6f (in the AFM state) does exhibit a three-peak structure,

though not of course with sharp peaks because of the small system size. The sum distribution roughly reflects what would be expected in a conventional coexistence state (see also Ref. [43]).

In the XXZ model very close to the isotropic point, we also expect remnants of the $O(3)$ symmetry (which in this case is exact at $\lambda = 0$). However, as we saw above in Sec. S8 A, in the XXZ model the magnetization jump at H_c is relatively much larger. Therefore, the length scale at which the $O(3)$ symmetry is violated should be much larger in the CBJQM for comparable distance from the $h = 0$ transition point. This distance can be taken as the transition field h_c in either model, or, equivalently, the spin gap at $h = 0$.

To further justify the emergent $O(3)$ symmetry in the CBJQM, we calculate the cross-correlation ratio

$$C_{xy,p} = \frac{\langle m_{xy}^2 m_p^2 \rangle}{\langle m_{xy}^2 \rangle \langle m_p^2 \rangle}, \quad (\text{S19})$$

where m_{xy}^2 is the squared off-diagonal (XY) AFM order parameter

$$\begin{aligned} m_{xy}^2 &= \frac{1}{2}(m_x^2 + m_y^2) \\ &= \frac{1}{4N^2} \sum_{i,j} (-1)^{i-j} (S_i^+ S_j^- + S_i^- S_j^+). \end{aligned} \quad (\text{S20})$$

The ratio (S19) measures the covariance between the AFM and PS order parameters and, thus, it can be used to detect the symmetry of the joint order parameter vector (m_x, m_y, m_z, m_p) . It is obvious that $C_{xy,p} = 1$ when m_{xy} and m_p are completely uncorrelated. Therefore, we expect the ratio to be close to 1 deep inside either the PS or the AFM phase. On the other hand, if the two order parameters are connected by an $O(3)$ symmetry, it is easy to see that the ratio should take the value of $3/5$, while if the symmetry is $O(4)$ the value is $2/3$. Similar cross-correlations were previously studied in the context of the DQCP with emergent $SO(5)$ symmetry [6, 9].

For $h = 0$, the AFM order parameter is inherently $O(3)$ symmetric and m_{xy}^2 in Eq. (S19) can be replaced by m_z^2 , which makes the entire correlation function diagonal in the S^z basis used in our SSE simulations. However, for $h > 0$ the operator m_{xy}^2 is off-diagonal and has to be treated in a different way using a string estimator, as explained in Sec. S1 F. These off-diagonal measurements are much noisier than the corresponding diagonal ones (also because the simulations overall are more challenging when $h > 0$), and we can therefore not reach as large system sizes for $C_{xy,p}$ as for the corresponding diagonal quantity $C_{z,p}$ at $h = 0$.

We first discuss $h = 0$, where emergent $O(4)$ symmetry was discovered in previous work by examining primarily the order-parameter distribution [7]. Results for the ratio $C_{z,p}$ are shown versus Q/J ($J = 1$) for several system sizes in Fig. S19a. Here we observe values tending clearly toward 1 in the AFM phase, $Q < Q_c$. The results are more affected by long autocorrelations in the PS phase,

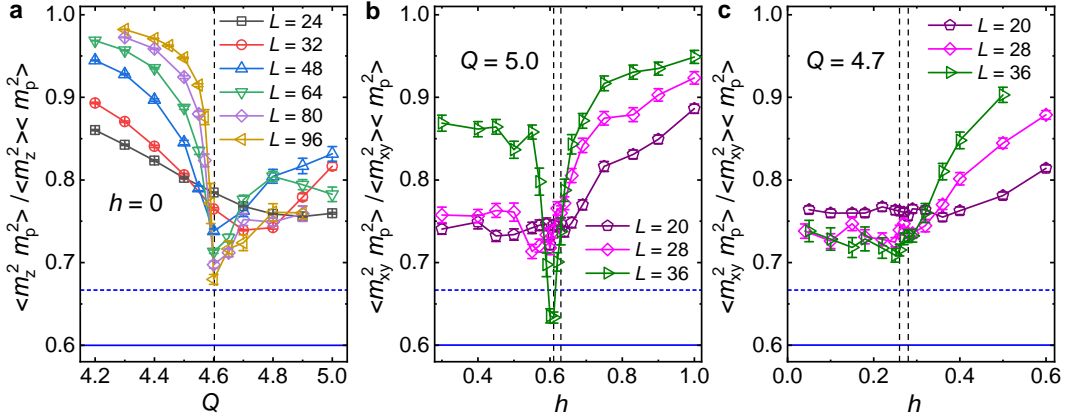


Figure S19. Field dependence of the cross-correlation ratio, Eq. (S19), for different system sizes. In a, results are shown vs Q at $h = 0$, where $m_{xy}^2 = (m_x^2 + m_y^2)/2$ can be replaced by m_z^2 thanks to the $O(3)$ symmetry of the AFM order parameter. In b and c, results are shown vs the field at fixed values of Q ; $Q = 5$ in b and $Q = 4.7$ in c. The horizontal lines are drawn at the values pertaining to $O(3)$ (solid lines) and $O(4)$ (dashed lines) symmetry. The vertical dashed lines indicate the previously determined transition points plus and minus their standard errors.

where the error bars, thus, are larger. The convergence toward 1 is also overall less obvious—there may be some non-trivial covariance between the long-ranged PS order parameter and the short-ranged AFM order parameter in the PS phase. The most important aspect of these results is the sharp minimum in $C_{z,p}$, which flows with increasing L toward a value of Q completely consistent with the known value $Q_c(h = 0) = 4.600$ [7]. The value of $C_{z,p}$ shows a significant size dependence, but, indeed, reaches close to the expected $O(4)$ value $C_{z,p} = 2/3$ for the largest system size, $L = 96$.

Next, we consider $Q > Q_c(h = 0)$ and scan the ratio $C_{xy,p}$ versus h . Fig. S19b shows results for three system sizes at $Q = 5$. Here we again observe a sharp minimum, especially for the largest system size, $L = 36$, where the minimum is located at $h \approx 0.61$. Considering that the trend with increasing L is a slight drift of the minimum toward larger values of h , the results are consistent with the transition point $h_c(Q = 5) = 0.62 \pm 0.01$ that we extracted from other quantities previously. The value of the ratio at the minimum is now below the $O(4)$ value for $L = 36$, and the trend with increasing L is to lower values. While the very high cost of simulations for larger L prohibit us from confirming that the $O(3)$ value is reached, the observed trends nevertheless support our assertion of emergent $O(3)$ symmetry.

Finally, in Fig. S19c we show results obtained at $Q = 4.7$, close to $Q_c(h = 0) = 4.6$. Here the minimum versus h is less sharp than in Fig. S19b and the values of the ratio are overall significantly higher when $h \approx h_c$. Comparing with the $h = 0$ results in Fig. S19a for Q close to the transition point, the values of $C_{z,p}$ are very similar for sizes $L \simeq 30$ to those of $C_{xy,p}$ when $h \approx h_c \approx 0.27$. We can explain this behavior as a symmetry cross-over effect: For very small $h > 0$, the system should initially, for moderate system sizes, behave as if $O(4)$ symmetry is emerging when $Q \rightarrow Q_c \approx Q_c(h = 0)$, while for larger

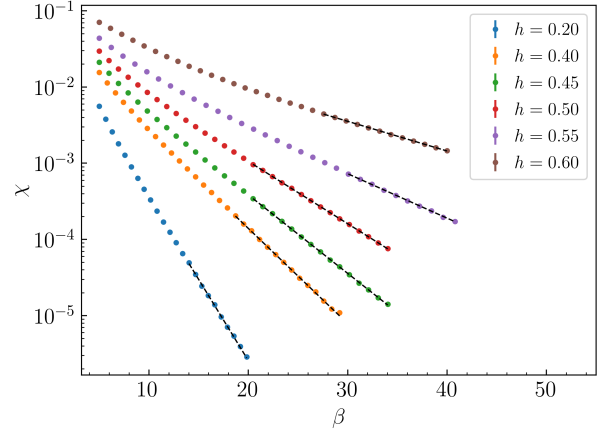


Figure S20. Uniform susceptibility versus the inverse temperature of the XXZ model with anisotropy parameter $\lambda = 0.1$ and several field values. The curves (almost straight lines) are fits to the full form in Eq. (S21), but the corrections to the leading exponential form are very small.

sizes the necessary effects of $h > 0$ to eventually take the symmetry of the AFM order parameter down from $O(3)$ to $O(2)$ will also imply violation of the $O(4)$ symmetry and flow of the ratio toward the smaller $O(3)$ value. Again, our systems are not sufficiently large to follow this behavior in its entirety, but, taken together, all results in Fig. S19 are certainly supportive of this $O(4) \rightarrow O(3)$ cross-over scenario.

C. Excitation gap

As discussed in the main text, the spin excitation gap closes linearly with the field, with no appreciable discontinuity at the transition, shown for $\text{SrCu}_2(\text{BO}_3)_2$ in

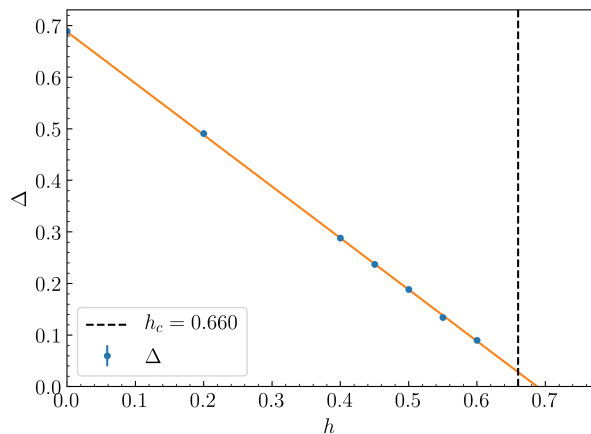


Figure S21. The spin gap of the XXZ model at $\lambda = 0.1$, extracted from the low-temperature uniform susceptibility as illustrated in Fig. S20. The vertical dashed line marks the first-order transition value h_c of the field, where the ground state changes discontinuously from one with $m = 0$ to one with $m > 0$ (as shown in Fig. S18). The gap to the $S^z = 1$ state for $h < h_c$ is of the form $\Delta(h) = \Delta(0) - h$, until the discontinuous jump to zero at h_c .

Fig. 6a and the CBJQM in Fig. 6c. We here provide details of the CBJQM gap calculation, and again also study the XXZ model as a benchmark.

We first extract the gap in the Ising phase of the anisotropic Heisenberg model from low-temperature behavior of the susceptibility, defined in Eq. (S5) and computed in the simulations in the standard way in terms of magnetization fluctuations according to Eq. (S6).

The Ising-like ground state is doubly degenerate in the thermodynamic limit, with a gap between the quasi-degenerate states closing exponentially as a function of the system size. When the system is locked in one of these ground states, which has total $S^z = 0$, and assuming a single band of excitations with $|S^z| = 1$ in momentum space with a quadratic minimum above the gap Δ , the susceptibility at low temperatures takes the form

$$\chi = \frac{Ae^{-\Delta\beta}}{1 + \beta^{-1}Ae^{-\Delta\beta}} \rightarrow Ae^{-\Delta\beta} \quad (\beta \rightarrow \infty), \quad (\text{S21})$$

where $\beta = J/T$ and A is a model dependent parameter.

Typical QMC results for χ , obtained with system sizes L up to 64, are graphed versus the inverse temperature $1/T$ ($J = 1$) in Fig. S20 on a lin-log plot, where the asymptotic exponential form corresponds to a straight line. We fit the data at low temperatures to the full functional form Eq. (S21). When using only the asymptotic form (which we do when analyzing the experimental data and also the CBJQM data below) the fits are still good and the extracted gaps only change insignificantly (which is reflected in the essentially straight fitted lines in the plot), as long as only data points at sufficiently low temperatures are included.

We graph Δ versus spin anisotropy λ in Fig. S21. As expected, the gap decreases linearly with the field, con-

sistent with the form $\Delta(h) = \Delta(0) - h$ expected when the lowest excitation has $S^z = 1$, and extrapolates to a point above the transition field h_c extracted in Fig. S18. Thus, the gap exhibits a discontinuous jump of about 0.04 in the thermodynamic limit.

We extract the PS gap of the CBJQM in the same way. The susceptibility computed at various fields for $Q = 5$ and system size $L = 48$ is shown in Fig. S22. For fields close to h_c ($0.6 \lesssim h \lesssim 0.62$), $\chi(T)$ first slightly increases with decreasing temperature, then forms a broad peak before decreases at sufficiently low temperatures. The low-temperature $\chi(T)$ data in the PS phase always follow a clear exponential decay in the PS phase, which we use here without corrections to extract $\Delta(h)$. The temperature has to be very low (and the system size very large) to reach the asymptotic behavior when h is close to h_c . The intricate behavior reflects a strong competition between the AFM and PS states close to the transition. The system size used here is sufficiently large for obtaining well-converged results for h up to 0.60, but we also show $h = 0.62$ results for reference.

The resulting gap for $h \leq 0.62$ is graphed in Fig. 6c in the main text. The strong fluctuating data and the narrow available temperature range of temperatures with exponentially decaying $\chi(T)$ prevent an accurate determination of the gap values close to h_c , as reflected in the corresponding large error bars in Fig. 6c. It is nevertheless clear that the gap discontinuity at h_c is small, though the relatively large uncertainty in the location h_c of the transition field of the CBJQM makes it impossible to obtain a meaningful estimate of the ratio of the gaps in the CBJQM and XXZ model (Fig. 6c versus Fig. S21). The dramatic difference in the magnetization jump (Fig. S18 versus S16) is much more obvious and may be a more prominent hallmark of the PS–AFM transition in the CBJQ model as well as in $\text{SrCu}_2(\text{BO}_3)_2$.

Our gap calculations for the CBJQM have focused on $Q = 5$, for which it is easier to obtain size-converged results than closer to the transition. Like the reduction of the magnetization jump when moving from $Q = 5$ to 4.7 in Fig. S16, the gap discontinuity should also be significantly reduced and be more similar to the barely discernible gaps observed at H_c in $\text{SrCu}_2(\text{BO}_3)_2$ at 2.1 and 2.4 GPa (Fig. 6a).

D. PS–AFM transition mechanism

The very different magnetization jumps point to a fundamental difference between the first-order phase transitions in the two models. When the magnetization per spin at a field immediately above h_c is large, as in the XXZ model at the anisotropy value $\lambda = 0.1$ studied here, there are hardly any remnants of the Ising-type order left in the ground state. The coexistence state can therefore not host any enhanced symmetry. In contrast, with the very small magnetization jump at h_c in the case of the CBJQM, the coexistence ground state still can have

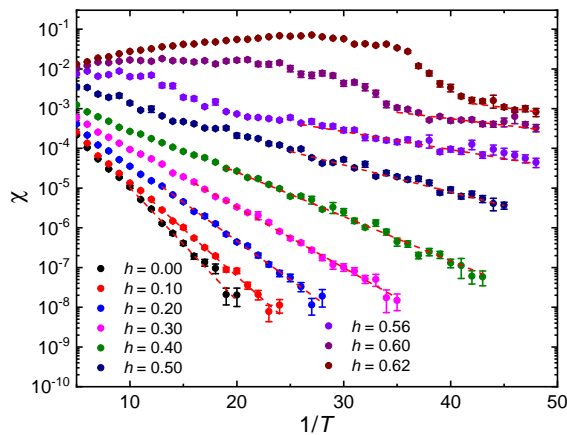


Figure S22. Uniform susceptibility of the CBJQM with $Q = 5$ computed for $L = 48$ and shown as a function of the inverse temperature at several different fields. The dashed lines are fits to the form $\chi \propto e^{-\Delta/T}$, which were used to extract the spin-gap vs h shown in Fig. 6c of the main text.

significant PS features left.

Our microscopic picture of the transition in the CBJQM is that the singlet PS ground state is associated with a tower of spin- S states, corresponding to successive excitations of plaquette singlets into triplets (triplons). In a field, an $S^z = S$ state corresponds to a number $n = S^z$ of triplons, or a volume fraction $\rho = S^z/L^2 = m$. Assuming that the interactions between the triplons are weak, states with different n all become almost degenerate at $h_c = \Delta(0)$ on account of the negative energy shifts $hS^z = hn$ of the $h = 0$ energies located at $\Delta_n = n\Delta_1$ above the $n = 0$ ground state.

In reality, we know that the interactions must be effectively weakly attractive, up to a certain density, so that a state with finite $n \propto L^2$ crosses the $S = 0$ PS ground state first, thus leading to the observed magnetization jump. However, given that the triplon (or magnetization) density is very small, $\rho \approx 0.0025$ in Fig. S16 at $Q = 5$ and $\rho \approx 0.001$ at $Q = 4.7$, these crossing states still can have significant PS character. Moreover, the “broken” triplet plaquettes can form increasing AFM order as the number of triplets n increases. The degeneracy of states with triplet density from zero to the transition value of ρ (which in our picture form the highly degenerate coexistence state) is consistent with a continuous symmetry of

the coexistence state, though we do not at present know the detailed mechanism by which the AFM order emerges from the broken plaquettes of the PS state and how the required O(3) Anderson rotor tower is realized. However, our observation of O(3) symmetry in the order-parameter histogram (Fig. 6e) demonstrates its existence.

Another way to qualitatively understand the emergent O(3) symmetry in the CBJQM is from the removal by the field of one of the AFM components of the emergent O(4) order-parameter vector at g_c when $h = 0$. This process simply corresponds to an O(4) model with an uniaxial deformation parameter, similar to λ in XXZ model, which takes the symmetry of the coexistence state at $h > 0$ down to O(3) by gapping out one of the AFM order-parameter components. This picture explicitly demonstrates the difference between the order parameter transformations in the two models: In the three-component XXZ model, the Ising order has to be explicitly destroyed in order to induce the AFM order. The Ising and XY AFM parts of the Hilbert space then are very different and must be separated by energy barriers. In the CBJQM, the transition just corresponds to a further infinitesimal deformation of the O(3) sphere, with the coexistence state having the full O(3) symmetry. The XY AFM order can be introduced gradually without complete destruction of the PS state, as described above, and a set of degenerate states with different S^z can establish a path for continuous changes (rotations) of the order parameter from PS to AFM without energy barriers. In reality, we know that the transition in the CBJQM also is ultimately conventionally first-order, but the idealized picture still describes the situation up to a large length scale, with detectable ramifications that we observe both in the CBJQM and in $\text{SrCu}_2(\text{BO}_3)_2$.

A further observation, based on Fig.S19 and the smallness of the magnetization jump, is that the coexistence phase also exhibits a cross-over from O(4) to O(3) symmetry even when transition field h_c is not very small. This robustness of O(4) symmetry (i.e., its persistence up to large length scales) supports our assertion that the DQCP point marked in Fig. 2 in the main text should be of the O(4) kind [38] even in the presence of the magnetic field. Strictly speaking, this point may exist as a true critical point only at $h = 0$, but with a very long correlation length and in practice realizing the DQCP phenomenology also at $h > 0$.

-
- [1] T. Senthil, A. Vishwanath, L. Balents, S. Sachdev, M. P. A. Fisher, *Science* **303**, 1490 (2004).
[2] A. W. Sandvik, *Phys. Rev. Lett.* **98**, 227202 (2007).
[3] T. Senthil, L. Balents, S. Sachdev, A. Vishwanath, M. P. A. Fisher, *Phys. Rev. B* **70**, 144407 (2004).
[4] H. Shao, W. Guo, A. W. Sandvik, *Science* **352**, 213 (2016).
[5] N. Ma, *et al.*, *Phys. Rev. B* **98**, 174421 (2018).
[6] A. Nahum, P. Serna, J. T. Chalker, M. Ortuño, A. M. Somoza, *Phys. Rev. Lett.* **115**, 267203 (2015).
[7] B. Zhao, P. Weinberg, A. W. Sandvik, *Nat. Phys.* **15**, 678 (2019).
[8] P. Serna, A. Nahum, *Phys. Rev. B* **99**, 195110 (2019).
[9] G. J. Sreejith, S. Powell, and A. Nahum, *Phys. Rev. Lett.* **122**, 080601 (2019).
[10] J. Takahashi, A. W. Sandvik, *Phys. Rev. Research* **2**, 033459 (2020).
[11] N. Xi, H. Chen, Z. Y. Xie, R. Yu, *arXiv:2111.07368*.

- [12] A. Nahum, J. T. Chalker, P. Serna, M. Ortuño, A. M. Somoza, *Phys. Rev. X* **5**, 041048 (2015).
- [13] C. Wang, A. Nahum, M. A. Metlitski, C. Xu, T. Senthil, *Phys. Rev. X* **7**, 031051 (2017).
- [14] B. Zhao, J. Takahashi, A. W. Sandvik, *Phys. Rev. Lett.* **125**, 257204 (2020).
- [15] D.-C. Lu, C. Xu, Y.-Z. You, *Phys. Rev. B* **104**, 205142 (2021).
- [16] W.-Y. Liu, *et al.*, *Sci. Bull.* **67**, 1034 (2022).
- [17] J. Yang, A. W. Sandvik, L. Wang, *Phys. Rev. B* **105**, L060409 (2022).
- [18] W.-Y. Liu, *et al.*, *Phys. Rev. X* **12**, 031039 (2022).
- [19] A. Keleş, E. Zhao, *Phys. Rev. B* **105**, L041115 (2022).
- [20] H. Shackleton, A. Thomson, S. Sachdev, *Phys. Rev. B* **104**, 045110 (2021).
- [21] Y.-H. Zhang, S. Sachdev, *Phys. Rev. B* **102**, 155124 (2020).
- [22] H. Kageyama, *et al.*, *Phys. Rev. Lett.* **82**, 3168 (1999).
- [23] S. Miyahara, K. Ueda, *Phys. Rev. Lett.* **82**, 3701 (1999).
- [24] S. Miyahara, K. Ueda, *J. Phys.: Condens. Matter* **15**, R327 (2003).
- [25] B. S. Shastry, B. Sutherland, *Physica B+C* **108**, 1069 (1981).
- [26] A. Koga, N. Kawakami, *Phys. Rev. Lett.* **84**, 4461 (2000).
- [27] P. Corboz, F. Mila, *Phys. Rev. B* **87**, 115144 (2013).
- [28] S. Haravifard, *et al.*, *Nat. Commun.* **7**, 11956 (2016).
- [29] M. E. Zayed, *et al.*, *Nat. Phys.* **13**, 962 (2017).
- [30] J. Guo, *et al.*, *Phys. Rev. Lett.* **124**, 206602 (2020).
- [31] J. Larrea Jiménez, *et al.*, *Nature* **592**, 370 (2021).
- [32] Y. H. Matsuda, *et al.*, *Phys. Rev. Lett.* **111**, 137204 (2013).
- [33] Methods, additional NMR data, data analysis, and supporting theoretical results are presented as Supplementary Information.
- [34] K. Kodama, *et al.*, *J. Phys. Condens. Matter* **14**, L319 (2002).
- [35] T. Waki, *et al.*, *J. Phys. Soc. Jpn.* **76**, 073710 (2007).
- [36] M. Takigawa, *et al.*, *J. Phys. Soc. Jpn.* **79**, 011005 (2010).
- [37] T. Moriya, *J. Phys. Soc. Jpn.* **18**, 516 (1963).
- [38] J. Y. Lee, Y.-Z. You, S. Sachdev, A. Vishwanath, *Phys. Rev. X* **9**, 041037 (2019).
- [39] C. Boos, *et al.*, *Phys. Rev. B* **100**, 140413 (2019).
- [40] S.-S. Gong, W. Zhu, D. N. Sheng, O. I. Motrunich, M. P. A. Fisher, *Phys. Rev. Lett.* **113**, 027201 (2014).
- [41] L. Wang, A. W. Sandvik, *Phys. Rev. Lett.* **121**, 107202 (2018).
- [42] Y. Nomura, M. Imada, *Phys. Rev. X* **11**, 031034 (2021).
- [43] G. Sun, N. Ma, B. Zhao, A. W. Sandvik, Z. Y. Meng, *Chin. Phys. B* **30**, 067505 (2021).
- [44] V. Y. Irkhin, A. A. Katanin, *Phys. Rev. B* **57**, 379 (1998).
- [45] Y. Q. Qin, *et al.*, *Phys. Rev. X* **7**, 031052 (2017).
- [46] A. V. Chubukov, S. Sachdev, J. Ye, *Phys. Rev. B* **49**, 11919 (1994).
- [47] A. P. Reyes, E. T. Ahrens, R. H. Heffner, P. C. Hammel, J. D. Thompson, *Rev. Sci. Instrum.* **63**, 3120 (1992).
- [48] M. Yogi, *et al.*, *J. Phys. Soc. Jpn.* **80**, SA027 (2011).
- [49] S. Allenspach, *et al.*, *Phys. Rev. Res.* **3**, 023177 (2021).
- [50] O. F. Syljuåsen, A. W. Sandvik, *Phys. Rev. E* **66**, 046701 (2002).
- [51] A. Dorneich, M. Troyer, *Phys. Rev. E* **64**, 066701 (2001).
- [52] K. Kodama, *et al.*, *J. Phys.: Condens. Matter* **17**, L61 (2005).
- [53] H. Kageyama, *et al.*, *J. Phys. Soc. Jpn.* **67**, 4304 (1998).
- [54] Z. Shi, *et al.*, *Nat. Commun.* **13**, 2301 (2022).
- [55] A. W. Sandvik, B. Zhao, *Chin. Phys. Lett.* **37**, 057502 (2020).
- [56] S. Sachdev, *Quantum Phase Transitions* (Cambridge University Press, New York, NY, 2011).
- [57] A. W. Sandvik, *AIP Conf. Proc.* **1297**, 135 (2010).
- [58] A. Sen, H. Suwa, A. W. Sandvik, *Phys. Rev. B* **92**, 195145 (2015).
- [59] W. Hong, *et al.*, *Phys. Rev. Lett.* **126**, 037201 (2021).
- [60] P. Sengupta, A. W. Sandvik, and R. R. P. Singh, *Phys. Rev. B* **68**, 094423 (2003).
- [61] In a 2D Heisenberg model with nearest-neighbor couplings J , we simply have $J_{2D} = J$. However, competing in-plane couplings, frustration in particular, can lead to a smaller effective value of J_{2D} .
- [62] P. Henelius and A. W. Sandvik, *Phys. Rev. B* **62**, 1102 (2000).
- [63] S. Wessel, I. Niesen, J. Stapmanns, B. Normand, F. Mila, P. Corboz, and A. Honecker, *Phys. Rev. B* **98**, 174432 (2018).
- [64] J. M. Kosterlitz, D. R. Nelson, M. E. Fisher, *Phys. Rev. B* **13**, 412 (1976).